Pericyte degeneration leads to neurovascular uncoupling and limits oxygen supply to brain

Kassandra Kisler[1,*], **Amy R. Nelson**[1,*], **Sanket V. Rege**[1,*], **Anita Ramanathan**[1], **Yaoming Wang**[1], **Ashim Ahuja**[1], **Divna Lazic**[1,2], **Philbert S. Tsai**[3], **Zhen Zhao**[1], **Yi Zhou**[4], **David A. Boas**[5], **Sava Sakadžić**[5], and **Berislav V. Zlokovic**[1]

[1]Department of Physiology and Biophysics and the Zilkha Neurogenetic Institute, Keck School of Medicine of the University of Southern California, Los Angeles, CA 90089

[2]Department of Neurobiology, Institute for Biological Research, University of Belgrade, 11060 Belgrade, Republic of Serbia

[3]Department of Physics, University of California, San Diego, La Jolla, CA 92093

[4]Department of Neurobiology, Chongqing Key Laboratory of Neurobiology, Third Military Medical University, Shapingba District, Chongqing, China, 400038

[5]Optics Division, Athinoula A. Martinos Center for Biomedical Imaging, Department of Radiology, Massachusetts General Hospital and Harvard Medical School, Charlestown, MA 02129

Abstract

Pericytes are perivascular mural cells of brain capillaries that are positioned centrally within the neurovascular unit between endothelial cells, astrocytes and neurons. This unique position allows them to play a major role in regulating key neurovascular functions of the brain. The role of pericytes in the regulation of cerebral blood flow (CBF) and neurovascular coupling remains, however, debatable. Using loss-of-function pericyte-deficient mice, here we show that pericyte degeneration diminishes global and individual capillary CBF responses to neuronal stimulus resulting in neurovascular uncoupling, reduced oxygen supply to brain and metabolic stress. We show that these neurovascular deficits lead over time to impaired neuronal excitability and neurodegenerative changes. Thus, pericyte degeneration as seen in neurological disorders such as Alzheimer's disease may contribute to neurovascular dysfunction and neurodegeneration associated with human disease.

Address correspondence: Berislav V. Zlokovic, M.D., Ph.D., Zilkha Neurogenetic Institute, 1501 San Pablo Street, Los Angeles, CA 90089, Phone: 323.442.2722 / Fax: 323.666.2184, zlokovic@usc.edu.
*These authors contributed equally to this work

INTRODUCTION

A properly functioning central nervous system requires regulation of cerebral blood flow (CBF) and oxygen supply to match neuronal functional activity, known as neurovascular coupling[1–3]. Neurovascular coupling is regulated by synchronous action of different cell types within the neurovascular unit including neurons, vascular smooth muscle cells, endothelium and astrocytes[4,5]. Pericytes, mural cells of the capillary vessel wall[6], play a critical role in the stabilization of the capillary wall[7–9], maintenance of the blood-brain barrier[10–12] and have been implicated in the regulation of capillary diameter and CBF[13–15]. Recent studies have demonstrated pericyte contractility in perfused brain slices including contractile responses to different pharmacological vasoactive agents and electrophysiological stimulation[13–15]. Moreover, has also been shown that active neurons increase their energy supply by dilating nearby arterioles and capillaries, and that capillaries dilate ahead of arterioles *in vivo* in response to neuronal stimulus[14,15]. Neuronally evoked capillary dilation *in vivo*, but not arteriolar dilation, has recently been shown to depend on a rise in intracellular calcium $[Ca^{2+}]_i$ in astrocytes[15].

Some studies, however, dispute the proposed physiological role of pericytes in neurovascular coupling. One study showed pericyte contractility to vasoconstrictors *in vivo*, but suggested that pericytes play insignificant role in neurovascular coupling[16]. The other study using genetically encoded microvascular mural cell labeling, functional calcium imaging and optogenetic light-driven cell activation showed that spontaneous cardiac and respiratory-driven cerebral vasomotion and calcium currents are detectable only in arterioles but not in capillaries, that smooth muscle cells but not pericytes constrict vessels after light stimulation, and that capillary dilation in response to neuronal stimuli is not substantial, thus concluding that pericytes do not contribute to regulation of CBF responses[17].

Pericyte degeneration is found in multiple neurodegenerative disorders exhibiting early neurovascular dysfunction[2,3,18] including mild dementia[19], Alzheimer's disease[20–23], and amyotrophic lateral sclerosis[24]. Additionally, it has been shown that pericytes die after ischemic stroke and constrict capillary blood flow during the reperfusion phase of stroke[14,25]. Therefore, elucidating whether pericyte degeneration contributes to CBF dysregulation and neurovascular dysfunction, as seen in these neurological disorders, is extremely important. Moreover, blood oxygen level-dependent (BOLD) functional imaging signals that depend on neurovascular coupling are typically abnormal in early stage Alzheimer's disease reflecting CBF dysregulation and aberrant hemodynamic responses, as shown by numerous studies[26]. Whether pericyte degeneration contributes to changes in BOLD signals in early Alzheimer's remains, however, presently unknown.

To address whether pericyte degeneration affects neurovascular coupling, we studied hemodynamic responses in loss-of-function pericyte-deficient platelet-derived growth factor receptor-β (*Pdgfrβ*$^{+/−}$) mice, which at a young age develop a moderate 25% loss of pericyte coverage of the brain capillary wall[12]. Given that the vast majority of cortical vasculature in mice is composed of capillaries[27], we hypothesized that if pericytes contribute to neurovascular coupling then *Pdgfrβ*$^{+/−}$ mice[12] will have reduced hemodynamic responses

and diminished oxygen supply after neuronal stimulation, which over time will compromise neuronal function leading to neurodegenerative changes.

RESULTS

Impaired global and individual capillary responses

First, we found that the global CBF response to a hind limb electrical stimulus determined by laser doppler flowmetry (LDF)[28] in young 1–2 month old *Pdgfrβ*^{+/−} mice compared to age-matched littermate *Pdgfrβ*^{+/+} controls was reduced by 30% (Fig. 1a, 95% confidence interval (CI) of the mean difference [lower bound, upper bound] [4.9, 54.9]; Cohen's d (d) = 1.15). Next, we used *in vivo* two-photon laser scanning microscopy (TPLSM) in *Pdgfrβ*^{+/−} mutants and controls to examine responses of individual capillaries (< 6 μm in diameter) and arterioles (7–25 μm in diameter including both pre-capillary and small penetrating arterioles) to a shorter-lasting electrical hind limb stimulus in a well-defined S1 cortical region (Fig. 1b) determined to be responsive by intrinsic optical signal (IOS) imaging. First, we applied a low-pass and notch filter to all individual time courses of capillary responses to minimize cardiac and respiratory vasomotion artifacts (Fig. 1c), and then captured the time courses of diameter increase in each capillary by fitting a sigmoid parametric function to the individual capillary data traces in each animal (Supplementary Fig. 1). We computed time to 50% peak capillary dilation by averaging responses within individual animals and comparing data across animals (Fig. 1d, Supplementary Fig. 1). We found that capillaries in *Pdgfrβ*^{+/−} animals responded with a 6.5 s delay (95% CI [−8.6, −4.4], d = 2.69) in reaching 50% peak capillary dilation compared to *Pdgfrβ*^{+/+} age-matched littermate controls (Fig. 1d; see Methods for details of diameter measurements), whereas the time to 50% peak arteriolar dilation was not different between the two groups (Fig. 1e,f; 95% CI [−4.2, 2.5], d = 0.25). Consistent with previous reports[14,15], we found that in control *Pdgfrβ*^{+/+} mice arterioles reached 50% peak dilation with a delay of 2 s in average compared to capillaries that dilated first (95% CI [−4.2, −0.1], d = 0.92). In contrast, vessel responses in *Pdgfrβ*^{+/−} mutants had the opposite order of dilation with capillary diameter increases lagging behind arteriolar diameter increases by 3.5 s in average (95% CI [0.2, 6.8] d = 1.02).

Immunostaining analysis of CD13-positive pericytes in the stimulated cortical S1 area in a subset of control *Pdgfrβ*^{+/+} mice studied for capillary dilation indicated a 77% pericyte coverage of lectin-positive endothelial profiles (< 6 μm in diameter) (Supplementary Fig. 2a–c), consistent with previous reports[8,11,12]. Young pericyte-deficient *Pdgfrβ*^{+/−} mutants compared to age-matched littermate controls had approximately 29% reduction in pericyte coverage reflecting a 22% absolute loss of pericyte coverage (Supplementary Fig. 2a,b; 95% CI [17.7, 26.6], d = 7.16), as reported[12]. Consistent with a delay in capillary diameter increases (Fig. 1c,d), analysis of TPLSM capillary linescans[29] (Fig. 1g) indicated 55% delay in stimulus-driven red blood cell (RBC) flow velocity increase in capillaries of *Pdgfrβ*^{+/−} mice compared to *Pdgfrβ*^{+/+} controls (Fig. 1h–i; 95% CI [−104.9, −6.0], d = 1.08). Importantly, there was no difference in the basal arteriolar or capillary vessel diameter between *Pdgfrβ*^{+/−} and *Pdgfrβ*^{+/+} animals (Supplementary Fig. 3a; arterioles – 95% CI [−3.8, 2.9], d = 0.12; capillaries – 95% CI [−0.5, 0.2], d = 0.47), indicating that anatomical changes in the vessel diameter prior to stimulation did not influence vessel responses.

Similarly, there were no baseline differences before stimulation between RBC flow velocity in arterioles or capillaries between $Pdgfr\beta^{+/-}$ and $Pdgfr\beta^{+/+}$ animals (Supplementary Fig. 3b; arterioles – 95% CI [−1.2, 1.0], d = 0.13; capillaries – 95% CI [−0.2, 0.3], d = 0.14). The smooth muscle thickness in diving arterioles was also similar in $Pdgfr\beta^{+/+}$ and $Pdgfr\beta^{+/-}$ mice as shown by smooth muscle cell actin staining (Supplementary Fig. 3c,d; 95% CI [−1.1,0.4], d = 0.64).

To assess whether loss of pericyte coverage was directly responsible for the loss of capillary dilation, we took advantage of the natural "mosaic" situation of the present murine model where some segments of the capillary bed lack pericytes while the others are covered by pericytes. We crossed $Pdgfr\beta^{+/-}$ mice with NG2-dsRed mice ($Pdgfr\beta^{+/-}$; dsRed) to identify pericyte-covered capillaries. NG2-dsRed mice express dsRed in pericytes, smooth muscle cells, and oligodendrocyte progenitor cells[14]. These mice have been used previously to elucidate the role of capillary vasodilatation *in vivo* and to identify pericyte-covered microvessels[14]. We determined capillary responses in $Pdgfr\beta^{+/-}$;dsRed mice, and measured the diameter changes of capillaries where dsRed-labeled pericytes were present (either somata or processes; responses did not differ significantly at these locations) and where no pericyte coverage was visible. Upon stimulation, active dilation of capillaries lacking pericyte coverage was barely detectable after 3 s compared to those with pericyte coverage that showed significant dilation in response to a stimulus (Fig. 1j,k, Supplementary movies 1 and 2; 95% CI [0.2, 2.1], d = 1.38). These data suggest that capillaries lacking pericyte coverage in pericyte-deficient mice do not actively relax to generate the capillary dilation in contrast to capillaries covered by pericytes, altogether indicating that the lack of pericyte coverage likely leads to neurovascular uncoupling.

To investigate further whether young 1–2 month old pericyte-deficient mice compared to controls develop a global deficit in neurovascular coupling, we studied changes in IOS acquired under 530 nm illumination. IOS at this wavelength has been demonstrated to reflect changes in hemodynamic responses[30,31]. As illustrated by representative IOS images and traces, pericyte-deficient mice compared to controls show reductions in the peak signal amplitude and time to peak stimulus response (Fig. 2a, b) with an average 36% decrease in the peak amplitude (Fig. 2c; 95% CI [2.6, 70.5], d = 1.25) and a 2 s delay in 50% time to peak (Fig. 2d; 95% CI [−2.8, 0.2], d = 1.04) confirming abnormal neurovascular coupling. Importantly, neuronal activity assessed by *in vivo* local field potential (LFP) recordings in somatosensory cortex of the same mice indicated no difference in the shape, amplitude or slope of the LFPs (Fig. 2e–h; amplitude – 95% CI [−0.1, 0.1], d = 0.04; slope – 95% CI [−0.2, 0.2,], d = 0.16) after hind limb stimulation, demonstrating that neuronal activity is unchanged in 1–2 month old $Pdgfr\beta^{+/-}$ mice. These data provide evidence for impaired hemodynamic responses in pericyte-deficient mice at an early stage when neuronal excitability is still normal.

Normal arteriolar responses and endothelial-dependent vasodilaton

We next studied whether changes in the arteriolar responses and endothelial-dependent vasodilation can contribute to neurovascular uncoupling in young $Pdgfr\beta^{+/-}$ mice. Consistent with a comparable time to 50% peak arteriolar dilation (Fig. 1f), the stimulus-

driven RBC velocity increase in arterioles was also similar in 1–2 month old *Pdgfrβ*^{+/−} and *Pdgfrβ*^{+/+} mice (Fig. 3a; 95% CI [−2.0, 4.1], d = 0.38). We then imaged Alexa 633-positive arterioles in the S1 cortical region using acute brain slices from *Pdgfrβ*^{+/+} and *Pdgfrβ*^{+/−} mice (Fig. 3b–e). Arteriolar constriction in response to phenylephrine was unchanged in *Pdgfrβ*^{+/−} arterioles compared to *Pdgfrβ*^{+/+} arterioles (Fig. 3c,d; 95% CI [−5.7, 14.7], d = 0.71). Similarly, there was no difference in smooth muscle relaxation induced by adenosine, an endothelium-independent vasodilator that acts as a direct vascular smooth muscle cell relaxant[32], in *Pdgfrβ*^{+/+} and *Pdgfrβ*^{+/−} arterioles pre-constricted with phenylephrine (Fig. 3c,e; 95% CI [−12.1, 17.2], d = 0.29). We then tested *in vivo* the effect of adenosine, and found no changes in CBF responses between *Pdgfrβ*^{+/−} mice and littermate controls, as determined by LDF using methods as previously reported[32] (Fig. 3f; 95% CI [−5.7, 11.7] d = 0.78). These data show that the smooth muscle cell function is unaffected in *Pdgfrβ*^{+/−} mice and therefore does not contribute to neurovascular uncoupling.

We also studied the effects of endothelium-dependent vasodilators acetylcholine for receptor-mediated vasodilation and the calcium ionophore A23187, a compound that produces endothelium-dependent vasodilation through receptor-independent mechanisms[32], and found no changes in CBF responses between *Pdgfrβ*^{+/−} mice and *Pdgfrβ*^{+/+} littermates (Fig. 3g,h; acetylcholine – 95% CI [−18.9, 11.3], d = 0.57; A23187 – 95% CI [−6.9, 1.2], d = 1.61), suggesting that the endothelial signaling is still intact at early stages in *Pdgfrβ*^{+/−} mice, and can thus provide retrograde propagation of dilatory signals through the endothelium[18].

Since alterations in neurovascular coupling might result from a cascade of alterations between trophically interdependent cells within the neurovascular unit we have analyzed astrocyte coverage of microvessels, the number of astrocytes and microglia and total microvascular length in 1–2 month old *Pdgfrβ*^{+/−} mice. Immunostaining for two astrocyte markers - aquaporin-4 and glial fibrillar acidic protein (GFAP) - indicated no detectable changes in astrocyte coverage of the microvessel walls (e.g., normal coverage by aquaporin-4-positive endfeet) and astrocyte numbers (GFAP-positive astrocytes) (Supplementary Fig. 4a,b,c; AQP4 – 95% CI [−44.5, 14.1], d = 0.15; GFAP – 95% CI [−10.6, 4.5], d = 0.60) consistent with a previous report showing no detectable changes in astrocytes in *Pdgfrβ*^{+/−} mice at 6–8 months of age[12]. These data also suggest that the astrocyte-dependent component of CBF regulation is likely intact at early stages in *Pdgfrβ*^{+/−} mice. Similarly, there was no change in microglia number as shown by microglia-specific Iba1 immunostaining (Supplementary Figure 4a,d; 95% CI [−5.1, 4.1], d = 0.16). As reported, an increase in microglia is seen in *Pdgfrβ*^{+/−} mice only at a very late stage at 14–16 months of age, but not before[12]. Collectively, these studies suggest no detectable changes in endothelial, smooth muscle cell-dependent and astrocyte-dependent mechanisms of flow regulation in the present pericyte-deficient model.

3D reconstructions of the vasculature revealed 10–16% lower capillary density in layers I-VI of the somatosensory cortex that while did not reach significance suggested vascular capillary phenotype in *Pdgfrβ*^{+/−} mice compared to *Pdgfrβ*^{+/+} controls (Supplementary Figure 4e,f; 95% CI [−6.2, 38.8], d = 1.25 for capillary density), as reported[12]. In contrast, no changes were found in larger cortical vessels including the arterioles (Supplementary

Figure 4e,f; 95% CI [−140.3, 152.5], d = 0.07). To determine whether moderate microvascular reductions affect hemodynamic responses independently of pericyte coverage, we utilized another transgenic murine model with microvascular reductions but normal pericyte coverage, i.e., haploinsufficient mesenchyme homeobox 2 (*Meox2*^{+/−}) mice[33]. *Meox2*^{+/−} mice display approximately 30% reduction in the cortical capillary density due to primary endothelial hypoplasia, but have normal global CBF responses to neuronal stimulus[12]. We confirmed reduced capillary density and normal pericyte coverage in *Meox2*^{+/−} mice (Supplementary Fig. 5a–c; capillary length – 95% CI [30.4, 39.8], d = 16.94; pericyte coverage – 95% CI [−11.6, 15.3], d = 0.20), and showed that these mice have normal stimulus-driven capillary and arteriolar responses as determined by TPLSM (Supplementary Fig. 5d–e; capillary – 95% CI [−1.8, 0.66], d = 0.91; arteriole – 95% CI [−2.8, 1.2], d = 0.70), consistent with previously reported normal global CBF responses[12]. Whether additional compensatory mechanisms can contribute to normal global hemodynamic responses in *Meox2*^{+/−} mice despite reductions in capillary length[12] remains unknown. However, the analysis of vessel responses in *Pdgfrβ*^{+/−} and *Meox2*^{+/−} mice suggests that a moderate reduction in capillary density alone does not lead to aberrant neurovascular coupling unless mice develop pericyte deficiency, as seen in *Pdgfrβ*^{+/−} mutants.

Reduced tissue oxygenation and oxygen supply to brain under stimulus

Tight regulation of blood flow is critical for oxygen availability and normal brain function[1,3,18]. Therefore, changes in CBF responses due to pericyte degeneration could potentially create a state akin to chronic hypoperfusion or hypoxia[12] around the capillary-fed tissue, which may then lead to metabolic stress and accelerated neuronal damage and loss. To assess tissue oxygenation, we used *in vivo* TPLSM pO_2 (oxygen partial pressure) imaging in the cortex at two depths[34] (Fig. 4a). *Pdgfrβ*^{+/−} mice had an overall shift in tissue oxygenation to pO_2 values lower than the typical 20–40 mmHg range observed in normal mice (Fig. 4b). At 200 μm from the brain surface (Fig. 4a), a significant portion of the tissue in *Pdgfrβ*^{+/−} mice had low pO_2 values (< 15 mmHg) compared to *Pdgfrβ*^{+/+} controls (Fig. 4c: 100 μm – 95% CI [−7.7, −1.1], d = 3.01; 200 μm – 95% CI [−27.5, −10.0], d = 4.86). In particular, in tissue far from arterioles, *Pdgfrβ*^{+/−} mice exhibited even lower pO_2 (< 5 mmHg), indicating potential existence of chronically hypoxic tissue pockets (Fig. 4a).

To study how the tissue oxygen supply changes in response to hind limb stimulus, we next conducted IOS measurements acquired at 627 nm in young *Pdgfrβ*^{+/−} and *Pdgfrβ*^{+/+} mice. At this wavelength, light is dominantly absorbed by deoxy-hemoglobin and changes in IOS mainly reflect changes in oxygen consumption and/or delivery during hemodynamic response[30,31]. The initial dip (Fig. 4,d, e) is thought to be primarily the result of neuronal activity, i.e., increase in oxygen consumption increases deoxy-hemoglobin before a significant increase of CBF washes out deoxy-hemoglobin, but it is possible that it could also result from an initial increase in cerebral blood volume and total hemoglobin due to stimulus[30,31]. The positive peak (overshoot) (Fig. 4. d, e) is predominantly due to the deoxy-hemoglobin washout[31]. *Pdgfrβ*^{+/−} mutants compared to *Pdgfrβ*^{+/+} controls showed a 34% reduction in the IOS signal peak (overshoot) and a delay in time to peak (Fig. 4d,e,f; 95% CI

[15.8, 52.6], d = 2.92), indicating a reduction in oxygen delivery to the hind limb S1 cortex that supports the observed deficit in neurovascular coupling.

To corroborate these data, we studied reduced nicotinamide adenine dinucleotide (NADH) changes in response to hind limb stimulus. NADH is a molecule that is ubiquitously expressed and also intrinsically fluorescent in its reduced state, but not in its oxidized state (NAD$^+$) allowing it to function as a cellular metabolic indicator[35]. Astrocytes labeled with SR101 were used to control for the possible effect of hemodynamic changes due to stimulation on NADH fluorescence intensity[36] (Fig. 5a). TPLSM *in vivo* imaging of NADH revealed a significant transient NADH signal increase in *Pdgfrβ*$^{+/−}$ mice (compared to negligible change in *Pdgfrβ*$^{+/+}$ controls) during functional activation (Fig. 5b; 95% CI [−0.1, 0.0], d = 1.13), indicating a reduction in oxygen delivery compared to consumption. Together these data show that the capillaries in pericyte-deficient mice are incapable of supplying sufficient oxygen to brain either at rest or under stimulus.

We then sought to determine if the changes observed in CBF regulation and oxygen delivery compared to consumption paralleled changes in lactate metabolism. Lactate, produced by astrocytes, is considered an alternate fuel source for neurons, requiring less oxygen for energy production than glucose[37,38]. Using *in vivo* microdialysis of the somatosensory cortex, we found that 1–2 month old *Pdgfrβ*$^{+/−}$ mice exhibited a 47% higher interstitial fluid (ISF) level of lactate in the cortex than *Pdgfrβ*$^{+/+}$ littermate controls (Fig. 5c; 95% CI [−8.1, 102.7], d = 1.10), while the ISF glucose level (Fig. 5d; 95% CI [−65.9, 23.3], d = 0.66) and serum metabolite levels (Supplementary Fig. 6a,b: lactate – 95% CI [−24.1, 37.7] d = 0.32; glucose – 95% CI [−28.6, 30.7], d = 0.05) remained unchanged, likely reflecting a metabolic shift caused by insufficient oxygen supply. Moreover, upon neuronal stimulation via high [K+] retrodialysis, we found a significantly lower increase in stimulus-driven lactate levels in the ISF in *Pdgfrβ*$^{+/−}$ mice compared to controls by 28% (Fig. 5e; 95% CI [5.2, 50.5], d = 1.98), possibly reflecting increased utilization of lactate released from astrocytes by activated neurons in a setting of low oxygen when lactate becomes a preferred energy metabolite for neurons[38].

Impaired neuronal function and secondary neurodegeneration

Finally, we studied whether pericyte reductions causing early hemodynamic changes can lead to impaired neuronal function over time. As shown above, 1–2 month old *Pdgfrβ*$^{+/−}$ mice develop significant hemodynamic changes due to pericyte dysfunction, but do not show changes in neuronal excitability (Fig. 2e–h). Using voltage-sensitive dye (VSD) imaging of evoked membrane potential responses in the hind limb S1 cortical area, we confirmed a normal depolarization pattern with no abnormalities in peak amplitude of response or response latency in 1–2 month old *Pdgfrβ*$^{+/−}$ mice (Supplementary Fig. 7a–d: time to peak – 95% CI [−0.01, 0.05], d = 0.96 ; peak fluorescence change – 95% CI [−0.2, 0.2], d = 0.07). Structural analysis by dual labeling of neurons with NeuN (neuronal marker) and SMI-312-positive neurofilaments revealed a normal number of neurons and normal neuritic density in the S1 cortical area (Fig. 6a–c; NeuN – 95% CI [−222.0, 306.4], d = 0.23; neuritic density – 95% CI [−4.0, 5.4], d = 0.22) and hippocampus (not shown). Dual labeling for NeuN and terminal deoxynucleotidyl transferase dUTP nick end labeling (TUNEL) staining for DNA

fragmentation was negative (Fig 6a) demonstrating no detectable neuronal cell death at this early stage. Novel object recognition, nesting, and burrowing tests showed no behavioral deficits (Fig. 6d–f; NOR – 95% CI [−8.0, 22.7], d = 0.83; nest score – 95% CI [−0.4, 2.1], d = 1.55; food displaced – 95% CI [−80.7, 107.4], d = 0.18). However, 6–8 month-old *Pdgfrβ*^{+/−} mice displayed abnormalities in the evoked cortical depolarization, peak amplitude of response and response latency (Fig. 6g–j; time to peak – 95% CI [−0.2, 0.0], d = 1.21; peak fluorescence – 95% CI [−0.0, 0.3], d = 1.38), had significantly reduced neuron numbers in the S1 cortex and CA1 hippocampal subfield by 15% and diminished neuritic density by 22%, respectively (Fig. 6k–m; NeuN cortex – 95% CI [−0.2, 30.4], d = 1.93; NeuN hippocampus – 95% CI [−1.8, 31.9], d = 1.24; SMI-312 cortex – 95% CI [2.2, 43.6], d = 1.43; SMI-312 hippocampus – 95% CI [2.9, 41.6], d = 1.48), and exhibited occasional double positive TUNEL/NeuN cells (Fig. 6k) and changes in behavior (Fig. 6n–p; NOR – 95% CI [5.5, 30.8], d = 2.48; nest score – 95% CI [0.6, 1.4], d = 3.62; food displaced – 95% CI [15.4, 137.0], d = 2.76). Collectively these data suggest that pericyte-deficient mice develop age-related neurodegenerative changes as a continuum of the pathophysiological process initially triggered by pericyte degeneration.

As expected, global CBF responses to a stimulus progressively worsened in 6–8 month old, reduced by 58% relative to age matched controls (Supplementary Fig. 8a; 95% CI [49.7, 66.1], d = 12.22), compared to a 30% reduction in 1–2 month old *Pdgfrβ*^{+/−} mice (Fig. 1a), that could be attributed to both a progressive pericyte reduction at 6–8 months, i.e., 38% relative loss of coverage (Supplementary Fig. 8b,c; 95% CI [18.9, 56.8], d = 3.46) compared to 29% at 1–2 months (Supplementary Fig. 2a–b), and added secondary neuronal changes, as suggested by our data (Fig. 6g–m).

DISCUSSION

The present study shows that pericyte-deficient *Pdgfrβ*^{+/−} mice develop early-reduced global and individual capillary CBF responses to neuronal stimulus resulting in neurovascular uncoupling, limited oxygen supply to brain and metabolic stress. At this early stage characterized by impaired hemodynamic responses, we did not find detectable changes in neuronal, endothelial, smooth muscle cell-dependent and astrocyte-dependent mechanisms of flow regulation suggesting that pericyte dysfunction is the primary factor driving CBF dysregulation in this loss-of-function model. We cannot rule out, however, a possibility that moderate reductions in capillary cortical density (10–15%), although found to be insignificant in the present study, can still contribute indirectly to diminished global CBF responses in young *Pdgfrβ*^{+/−} mutants. On the other hand, our finding of delayed stimulus-driven individual capillary responses would support direct causality between pericyte deficiency and diminished capillary dilation in this model. We also show that impaired hemodynamic responses lead over time to impaired neuronal excitability and secondary neurodegenerative changes. Thus, at a later stage, dysfunction in other neurovascular unit cell types including neurons may contribute indirectly to worsen abnormal hemodynamic responses initiated by pericyte degeneration.

It is conceivable that other vascular changes such as blood-brain barrier breakdown and accumulation of blood-derived toxic products in the brain[10–12], may contribute to neuronal

dysfunction and neurodegenerative changes seen with age in pericyte-deficient mice. The exact contributions of impaired hemodynamic responses and blood-brain barrier breakdown to the pathophysiological process of neurodegeneration remain, however, presently unknown.

Although extremely useful for understanding pericyte biology and providing important insights into their role in regulating neurovascular functions[7,9–12], the current models of PDGF-BB and PDGFRβ deficiency have their own limitations. For example, they cannot isolate the developmental impact of embryonic loss of PDGFRβ signaling on vascular phenotype in adult and aging brain. Additionally, smooth muscle cells also express PDGFRβ, which contributes to vascular phenotype in the embryonic central nervous system (CNS)[7,9]. On the other had, the role of pericytes and smooth muscle cells in adult brain could be different from their role in the embryonic CNS, as discussed[9,12]. The present study indicates, however, that smooth-muscle cell function and responses to vasodilators or constrictors are not altered in arterioles of young $Pdgfr\beta^{+/-}$ mice. This is consistent with findings of intact stimulus-driven arteriolar diameter increases and normal RBC velocity arteriolar increase, and lack of basal differences in the arteriolar and capillary vessel diameter or basal RBC flow between young mutants and controls, as we report. Some studies have suggested that PDGFRβ is expressed even by neuronal progenitors in the subventricular zone[39], which has not been confirmed by others in the embryonic CNS[40] or adult brain[12,41]. Nevertheless, the present study examines CBF responses in the cortex but not subventricular zone containing the neuronal progenitor pool.

Recent studies in $NG2$-Cre transgenic mice expressing channelrhodopsin 2 (ChR2) found that light-driven optogenetic stimulation leads to constriction of smooth muscle cell-covered arterioles, but does not have a significant effect on pericyte-covered capillaries[17]. Because this study was focused on constrictive responses of mural cells[17], it is difficult to make a direct comparison with the present findings focused on dilation of capillaries and arterioles in a loss-of-function model. Using an optogenetic stimulation causing a hyperpolarization of the mural cells followed by relaxation and dilation of the vessels would allow for more direct comparison with the present study. It has been suggested, however, that a controversy between the previous optogentic study in transgenic mice[17] and recent findings by others demonstrating pericyte contractility and capillary dilation responses in normal mice in $vivo$[14,15] might be attributed to a drift in pericyte definition, particularly renaming pericytes on precapillary arterioles[42] to smooth muscle cells[43].

Additionally, one wonders whether a threshold for optogenetic stimulation of ChR2 in smooth muscle cells and pericytes in $vivo$ is comparable between these two cell types in $NG2$-Cre expressing ChR2 mice[17]. Smooth muscle cells and pericytes are known to express different types and amounts of contractile proteins and Ca^{2+} channels[8,43,44] and therefore might have different thresholds for optogenetic stimulation. Interestingly, another recent optogenetic study focused in $Pdgfr\beta$-Cre transgenic mice expressing ChR2 has shown that strong two-photon optogenetic stimulation of pericytes leads to their contractility constricting capillary lumens and reducing RBC flow in $vivo$ (D.A. Hartmann, R.I. Grant and A.Y. Shih, Medical University of South Carolina, personal communication), opposite from the previous report in $NG2$-Cre expressing ChR2 mice[17]. Whether the differences in

optogenetic ChR2 stimulation of pericytes and contractility are model-dependent, optogenetic light stimulus source and duration-dependent, and whether different *Cre*-drivers can lead to differential ChR2 expression in different pericyte subpopulations, remains to be determined by future studies. However, our present data in control, non-transgenic mice corroborate recent findings by others by showing that upon longer-lasting electrical forepaw stimulation capillaries dilate ahead of arterioles *in vivo*[15] consistent with the previous work showing that the same holds true after whisker stimulation[14]. These findings all together are consistent with several reports demonstrating Ca^{2+}-dependent pericyte contractility[13,14,45–48].

In contrast to all previous studies, the present study uses a *loss-of-function* approach to examine the effect of a loss of pericyte function on cerebrovascular regulation. We demonstrate that pericyte reductions lead to early hemodynamic cerebrovascular changes prior to changes in neuronal excitability and structure and/or changes in function of other neurovascular unit cell types, which links pericyte reductions to an age-dependent continuous pathophysiological process of neurodegeneration. Therefore, pericyte degeneration as seen in neurological disorders[19–24] associated with neurovascular dysfunction, such as Alzheimer's disease[2,3,18], can contribute to impaired neurovascular coupling and diminished oxygen supply to brain, as shown by BOLD signal changes early in the disease[26]. These hemodynamic changes, in turn, may contribute to neurodegeneration accompanying human disease. Thus, pericytes could be an important new therapeutic target to treat neurovascular dysfunction and neurodegeneration.

Methods

Animals

Pdgfrβ^{+/−} mice and their littermate controls on mixed 129S1/SvlmJ background were generated as we previously described[9]. All experiments were performed on 1–2 month old or 6–8 month old *Pdgfrβ*^{+/−} mice and littermate *Pdgfrβ*^{+/+} controls unless otherwise specified. *Pdgfrβ*^{+/−} mice with pericytes expressing dsRed (*Pdgfrβ*^{+/−};dsRed) were generated by crossing *Pdgfrβ*^{+/−} mice with NG2-dsRed mice on C57Bl6 background[11]. *Meox2*^{+/−} mice and their controls on C57Bl6 background were generated as we previously described[28] were used at 1–2 mo of age. Both male and female animals were used throughout the experiments. Mice were housed in plastic cages on a 12 h light cycle with ad libitum access to water and a standard laboratory diet. During *in vivo* surgery and experiments, body temperature was maintained with electric heating pads with thermal feedback and respiration monitored. Intraperitoneal injections of 5% glucose in isotonic saline (0.2 mL/25 g) were administered every two hours. Most experiments were performed under isofluorane anesthesia (SomnoSuite, Kent Scientific), unless otherwise specified. For details see specific experiments below. All procedures were approved by the Institutional Animal Care and Use Committee at the University of Southern California with National Institutes of Health guidelines and the Massachusetts General Hospital Subcommittee on Research Animal Care.

Cranial Window

Animals were initially anesthetized with 100 mg/kg of ketamine and 50 mg/kg of xylazine, then fixed in a stereotaxic frame (Kopf Instruments) and transitioned to isoflurane anesthesia. A circular cranial window was drilled over the hind limb region of the somatosensory cortex (center at AP = −0.94 mm, L = 1.5 mm). The window was filled with 2% low melt agarose (Sigma, A9539) in artificial cerebrospinal fluid (aCSF) and covered with a 3 mm round coverslip. Animals were maintained on isoflurane anesthesia for subsequent experiments.

Laser-doppler flowmetry (LDF)

CBF responses to hind-limb stimulation in anesthetized mice (~2% isoflurane) were determined using laser-Doppler flowmetry measured through a cranial window, as previously described[23,49]. The tip of the laser-Doppler probe (Transonic Systems Inc., Ithaca, NY) was stereotaxically placed 0.5 mm above the cranial window over the area determined to be responsive from IOS imaging (see below). CBF was recorded from the somatosensory cortex hind-limb region following electrical stimulation of the hind limb using a 60 s long stimulus. The percentage increase in CBF due to stimulation was obtained by subtracting the baseline CBF from the stable maximum plateau value reached during stimulus, and averaged over three trials per mouse.

For CBF response to drug application, the LDF probe was placed stereotaxically over the center of an open cranial window (center at AP = −0.94 mm, L = 1.5 mm). Drugs (10 μM Acetylcholine, 3 μM A23187, and 400 μM Adenosine, all from Sigma) were superfused individually over the window, and responses recorded as previously described[27].

In Vivo Two-Photon Microscopy

Diameter and Velocity Measurements—To identify the brain region responsive to hind limb stimulation for two-photon microscopy diameter and velocity experiments, red (630 nm) intrinsic optical signaling (IOS, see below) images were acquired in response to a 0.3 s electrical stimulus delivered to the contralateral hind limb at 5 V at a rate of 7 Hz, 5 ms pulse duration (6002 Stimulator, Harvard Apparatus) using custom electrical probes. At the frequency used, this is equivalent to a single 5 ms pulse stimulus. These images were not used for data analysis.

Areas determined to be responsive from IOS imaging to hind limb stimulation were located in the TPLSM and used for subsequent imaging. Mean arterial blood oxygen saturation (SpO$_2$) and heart pulse rate were continuously monitored with a small-animal wrap transducer (TSD270B, Biopac Systems, Inc.) on the hind paw using an MP-150 Oxy200 (Biopac Systems, Inc.). The following physiological parameters were maintained under 1.8–2% isoflurane anesthesia: arterial SpO$_2$ = 92 ± 3 mmHg and 75 ± 15 beats per minute. The vasculature was labeled via retro-orbital or tail vein injection of 70 kDa FITC-dextran (0.1 mL of 10 mg/mL) and imaged through the cranial window. *In vivo* images and linescans were acquired at depths up to 400 μm below the pial surface using a custom-built Zeiss LSM 5MP multiphoton microscope coupled to a mode locked Ti:sapphire laser (Mai Tai Deep See; Spectra Physics) set to 800 nm, or a Nikon A1R multiphoton microscope coupled to a

mode locked Ti:sapphire laser (Insight DS+; Spectra Physics) set to 820 nm for FITC excitation. FITC emission was collected using a 500–550 nm bandpass filter. Arteries were identified at the brain surface by morphology and direction of blood flow, and then followed into the brain for imaging.

An electrical stimulus (10 s, 10 Hz, 2 ms pulse duration) was delivered to the contralateral hind paw using custom electrical probes. Stimulus delivery and coordination with imaging were accomplished using a Digidata 1550 and accompanying pClamp software (Molecular Devices).

For diameter measurements, linescans were taken perpendicular to the vessels at 8.14–15 Hz, generating an image of vessel diameter over time. Diameter line scans were analyzed as thresholded diameter vs. time images of each vessel with custom protocols written in Igor Pro 6 (WaveMetrics). First, images were smoothed with a 3×3 pixel Gaussian filter to remove noise, and thresholded using the Igor Pro built-in "fuzzy entropy" threshold routine to generate a black and white (binary) image of the vessel diameter vs. time. The Igor Pro custom analysis protocol identified the transitions between black/white and white/black in each line of the image, indicating the edges of the vessel, and then calculated the width of the vessel for each line in the image. The resulting diameter data was low-pass filtered (1 Hz cut off) and notch filtered (0.5 Hz), then smoothed with a 1 s window box filter. Subsequently, sigmoid parametric functions were then fit to the individual filtered vessel data traces to capture the overall time course of diameter increase and obtain the time to 50% peak vessel dilation data. Vessels with basal diameters < 6 μm were considered capillaries and were confirmed by immunostaining (see below) for endothelial-specific *Lycopersicon esculentum* lectin fluorescent staining to visualize brain capillary profiles and pericyte-specific marker CD13 and vascular smooth muscle cell actin (SMα) to be CD13-positive and SMα-negative. Vessels of basal diameter > 7 μm were considered arterioles (i.e., 7 – 25 μm basal diameter) and were confirmed by immunostaining (see below) to be SMα-positive and CD13-negative.

Vessels outside the 627 nm IOS response area were excluded from analysis. Vessels imaged within the 627 nm IOS response region (5–7 vessels, capillaries and arterioles, per animal on average) were analyzed. Based on the diameter analysis, any vessel that showed a focal drift occurring during the experiment, or if there were excessive breathing or movement artifacts were excluded. Only vessels with a diameter change larger than 1% after stimulus start were considered as responding vessels and taken for further analysis. Using these criteria, a total of 50–70% of vessels measured responded. Under these conditions, the average maximal diameter measured upon stimulus was approximately 2.5% above basal diameter.

For in vivo two-photon vessel diameter and velocity experiments, data from analyzed vessels were averaged together by mouse for statistical analysis.

For RBC velocity, linescans along the vessels were taken at a rate of 2.6 kHz[24]. Velocity data was analyzed using a MatLab algorithm as described[24] then low-pass filtered (1 Hz cut off) and notch filtered (0.5 Hz), then box filtered with a 1 sec window to remove heartbeat and breathing artifacts using custom written protocols in Igor Pro to automate the filtering

process. As for diameter analysis, sigmoid parametric functions were then fit to the individual filtered vessel data traces to capture the overall time course of velocity increase and obtain the time to 50% peak RBC velocity data. Igor Pro code can be made available upon request.

For presentation in figure 1c,e,h the data was normalized such that the average basal diameter or velocity was set to zero, and the maximum set to 1. Basal diameters or velocities were taken as the average diameter of the vessel during the 10 sec prior to stimulus. For supplemental movies, high magnification 512×512 pixel images were taken at 1.57 s/frame in the FITC channel only, after identification of dsRed pericyte covered and uncovered capillary regions. Resulting image stacks were 3D gaussian filtered and registered (StackReg, ridged body algorithm) in FIJI (Image J). The final movies were rendered in Photoshop (Adobe) and FIJI.

For experiments with $Pdgfr\beta^{+/-}$; dsRed mice, the laser was set to 900 nm. FITC signal was collected as above, and the dsRed signal was collected using a 570–640 nm band pass filter (Chroma). An electrical hind limb stimulus was delivered as above (10 Hz, 10 s, 2 ms pulse width). Since the capillaries of $Pdgfr\beta^{+/-}$ mice dilate slower than capillaries of control mice (Fig. 1d), we chose the timepoint of 3 s, prior to 50% diameter change occurrence in $Pdgfr\beta^{+/-}$ mice to specifically examine the active dilation of pericyte-covered capillaries vs. pericyte-uncovered capillaries (Fig. 1k).

Tissue Oxygen partial pressure (pO$_2$) measurements—Experiments were conducted as described previously[29]. Briefly, the 5–6 mo old $Pdgfr\beta^{+/-}$ or $Pdgfr\beta^{+/+}$ mice were anesthetized with isoflurane, then the femoral artery was cannulated to administer the dyes, to continuously monitor the blood pressure and heart rate, and to sample systemic blood gases (pCO$_2$ and pO$_2$) and pH. A tracheotomy was performed, and a cranial window with dura removed was made. Blood pressure, heart rate, temperature, and end-tidal pCO$_2$ were monitored continuously during both surgery and experiment. Oxygen-sensitive dye (PtP-C343) was pressure-injected into cortical tissue using a glass micropipette inserted ~400 μm below the cortical surface. The cranial window was then sealed with a glass coverslip and isoflurane was discontinued and replaced with alpha-chloralose. Mice were ventilated with a mixture of air and oxygen and the following physiological parameters were maintained: arterial pO$_2$ = 115 ± 15 mmHg, arterial pCO$_2$ = 37 ± 2 mmHg, mean arterial blood pressure = 100 ± 10 mmHg, and pH = 7.37 ± 0.02. A blood plasma was labeled by a small amount of FITC dye to obtain vascular images in the planes of pO$_2$ measurement to coregister later with the 3D vascular stacks. Tissue pO$_2$ was measured at 2 depths (100 μm and 200 μm from surface) at 800–1000 locations at each depth. At each pO$_2$ imaging location, we excited phosphorescence by trains of femtosecond pulses from a Ti:sapphire oscillator at 840 nm, gated by an electro-optic modulator, and acquired decays by averaging multiple excitation cycles. Each cycle consisted of a 10-μs excitation gate, followed by a 290 μs collection period. We averaged ~2,000 phosphorescence decays at each selected location for accurate pO$_2$ determination, resulting in 0.6 s per single-point pO$_2$ measurement. Blood plasma was subsequently labeled by Rhodamine dye to obtain vascular stack images.

NADH Measurements—NADH is intrinsically florescent with two photon excitation, and provides an indication of local tissue metabolism[30,31,50]. The tissue was also stained with sulforhodamine 101 (SR101) dye (Invitrogen), which preferentially loads into astrocytes and oligodendrocytes and acts as a control marker to correct for fluorescence changes due to hemodynamic changes in response to stimulation[31]. For these experiments, the window area was topically loaded with SR101 dye for 15 minutes prior to NADH imaging. Imaging was performed under isoflurane anethesia (1.8–2%) using the two-photon microscope described above through a cranial window at a depth of 50 μm under the same stimulus used for vessel diameter and velocity measurements. The TPLSM excitation set to 740 nm. NADH fluorescence emission was collected at 435–485 nm, and SR101 fluorescence emission was collected at 650–710 nm. Interleaved NADH and SR101 images were taken at a rate of 6.12 s/pair images at 50 μm depth. Images were loaded into Image J and ROIs were chosen so as to exclude the shadows of any large vessels. The SR101 signals were used to correct the average NADH ROI intensities for hemodynamic optical effects using a method reported previously[31].

Two-Photon 3D Angiograpy

Mice were anesthetized with isofluorane, then injected with 100 μL of 1mg/ml Alexa Fluor 594 lectin (Vector) into the femoral vein. After a 15 minute incubation, animals were transcardially perfused with 30 mL of PBS containing EDTA followed by 25 mL of 4% PFA in PBS at room temperature. The brain was removed, bisected down the midline, and cortices were separated from the rest of the brain. Cortices were placed between two microslides spaced 1.6 mm apart using metal washers and post-fixed in 4% PFA overnight. Cortices were then washed with 0.1 M PBS, and the somatosensory region extracted and embedded in a 4.5% agarose gel[51]. Brains were imaged at 1 μm steps using a 20x objective at 810 nm using a serial two-photon tomography microscopy as described[51].

Using custom scripts and plugins by Tissue Vision, images were processed in MatLab and stitched using Image J[51]. Projection images were made using Imaris x64 v8 (Bitplane Scientific Software). Blood vessels were traced in 50 μm deep increments through the depth of the cortex using the Vida Suite software package written for MatLab[52].

Voltage-sensitive dye (VSD) imaging

A cranial window was created over the hind-limb region in the somatosensory cortex. RH-1692 VSD (Optical Imaging) dissolved in aCSF was applied to the exposed cortex for 90 min[53]. The brain was then washed with aCSF and sealed with low-melt agarose and a coverslip as above. Under isofluorane anesthesia (~1.5%), images were captured at 5 ms/frame (184 × 124 resolution) using a 1/2 inch CCD MiCAM02-HR camera (SciMedia) coupled with MiCAM BV_ANA acquisition software. RH-1692 was excited using a MHAB-150W (Moritex Corp.) light source with a 632/22 filter, and fluorescence collected with a 665 nm long-pass filter. The contralateral hind-limb was stimulated by a brief mechanical vibration lasting 300 ms. Alternating image sets were taken with and without stimulus to generate "stimulus trial" and "baseline" responses. Next the baseline image set was subtracted from the stimulus trials to eliminate any background signal. 10 baseline subtracted trials were averaged to make up the final profile for each mouse. Time courses

were evaluated using a circular ROI centered over the hind-limb region as described previously[54]. Time courses were plotted using Igor Pro 6 and analyzed with Igor Pro 6 and Excel. Pseudocolor images for presentation were generated in Image J.

Intrinsic optical signal imaging (IOS)

IOS relies on changes in diffuse reflectance of the tissue due to changes in the tissue optical properties, notably changes in the blood volume and hemoglobin oxygen saturation[55]. Intrinsic optical signals were imaged through a cranial window. Under isofluorane anesthesia set at 1%, images were captured at 30 msec/frame using a 1/2 inch CCD MiCAM02-HR camera (SciMedia; 2x binned to 184 × 124 pixel resolution; 1 pixel = 16.5 μm) with accompanying BV_ANA acquisition software.

IOS imaging at 530 nm illumination—At 530 nm the absorption extinction coefficient of oxy- and deoxy-hemoglobin are equal[25,26]. Therefore, at this wavelength, optical absorption of blood is dominated by the total hemoglobin concentration (HbT), independent of oxygen content, reflecting cerebral blood volume (CBV)[26]. These changes also reflect CBF changes as CBV and CBF changes are strongly coupled[26]. Images were captured under a 530 nm green LED light source, and collected through a 522/36 nm band pass filter (Chroma). To match two-photon diameter and velocity stimulus conditions, images were acquired in response to a 10 s electrical stimulus delivered to the contralateral hind limb at 5 V at a rate of 10 Hz, 2 ms pulse duration (6002 Stimulator, Harvard Apparatus) using custom electrical probes. The resulting image sets were low pass filtered at 0.69 Hz, and the baselines corrected for any drift using the BV_ANA software. Signal time courses were evaluated using 13×13 pixel ROIs chosen in the region of peak signal change such that the regions did not include any large visible vessels, and were at least 30 μm away from any large vessels. Time courses were plotted using Igor Pro 6 and analyzed with Igor Pro 6 and Excel. Pseudocolor images for presentation were generated in Image J.

IOS imaging at 627 nm illumination—At 627 nm, optical absorption of blood is dominated by the deoxyhemoglobin (HbR) concentration [25,26,56]. Images were captured under a 627 nm red LED light source, and collected through a 640/40 nm band pass filter (Chroma). The contralateral hind limb was stimulated by a brief mechanical vibration lasting 300 ms. A total of 10 trials were performed and image data were averaged and stored for further quantification. To quantify the image results, customized Matlab scripts were used. A baseline frame was first obtained as the average of 10 frames (300 ms) before stimulation. For each 300 ms average frame (averaged from 10 frames) collected after stimulus onset, the intensity change was calculated relative to the baseline frame on a point-by-point basis. An adaptive 2D Wiener filter was applied to remove "salt & pepper" noise. Then, regions of interest (ROIs; 13×13 pixels) were chosen such that the regions did not include any large visible vessels, and were at least 30 μm from any large vessels, followed by quantification of the ROI intensity change over time.

In vivo electrophysiology

Following 530 nm IOS, electrophysiologic recordings were performed using custom-pulled borosilicate glass pipettes with filament (Sutter Instruments, outer diameter: 1.2 mm, inner

diameter: 0.69 mm) filled with sterile aCSF, attached to a CV-7B headstage (Axon Instruments), and mounted on a micromanipulator. The electrode was stereotaxically placed into Layer II (~200–300 μm deep) of the hindlimb somatosensory cortex at the peak responding location identified by 530 nm IOS. Data were acquired using a Multiclamp 700B amplifier and Digidata 1440A digitizer (Axon Instruments). Once the electrode was inserted, the depth was carefully adjusted so that the delivery of a single stimulus gave the maximal response. After recording a stable 10 second baseline, electrical hindlimb stimulus (10 Hz, 10 s, 5 V, 0.1 ms pulse duration) was applied. Local field potentials (LFPs) were acquired using pCLAMP Clampex 10.6 (Molecular Devices), and were subsequently filtered offline (2 to 300 Hz) and analyzed using pCLAMP Clampfit 10.6 software. For each 10 s stimulus trial, the 100 LFPs generated per trial were averaged into a single trace, and the slope of the initial deflection and peak LFP amplitude were quantified per trace. We performed 5–6 trials (replicates) per animal and data were averaged per each animal from 5 $Pdgfr\beta^{+/+}$ mice (25 experiments total, 2,500 LFPs) and from 6 $Pdgfr\beta^{+/-}$ mice (36 experiments total, 3,600 LFPs).

Immunohistochemistry

Mice were anesthetized with an i.p. injection of 100 mg/kg of ketamine and 50 mg/kg of xylazine, and transcardially perfused with 30 ml of phosphate buffer saline (PBS) containing EDTA followed by 30 ml of 4% PFA in PBS. Brains were removed and embedded into O.C.T. compound (Tissue-Tek) on dry ice, cryo-sectioned at a thickness of 18–20 μm. Sections were cut horizontally and those from depths of 50–150 μm, to coincide with TPLSM imaging depths, were used for analysis. Sections were subsequently blocked with 5% normal donkey serum (Vector Laboratories) with Triton (0.05%) for 1 hour and incubated in goat anti-CD13 (1:200) primary antibody diluted in blocking solution overnight at 4° C. To visualize CD13-positive pericytes, Dylight-649-conjugated donkey anti-goat (1:100) secondary antibody was used for incubation 1 hour at room temperature. To visualize brain microvessels, sections were incubated with 488-conjugated lectin (Vector Laboratories FL-1171, 1:200). To visualize smooth muscle, sections were incubated with Cy3-conjugated anti-SM-α (1:100) antibody. NeuN, TUNEL, Iba1, Aquaporin-4, and GFAP staining and reagents were described previously (see Supplementary Table 1). Sections were cover slipped using fluorescent mounting medium (Dako) and scanned using a Zeiss 510 meta confocal microscope with the following: 488 nm argon laser to excite Alexa Fluor 488, and emission collected through a 500–550 nm band pass (bp) filter; a 543 HeNe laser to excite Cy3, and emission collected through a 560–615 nm bp filter; a 633 HeNe laser to excite Dylight 649, and emission collected through a 650–700 nm bp filter. Z-stack projections and pseudo-coloring was performed using ZEN software (Carl Zeiss Microimaging).

Pericyte coverage analysis—Pericyte coverage analysis was performed as previously described[9,57]. Briefly, CD13 and lectin staining was performed in PFA fixed tissue sections as described above and signals from microvessels were separately subjected to automated threshold processing using Image J. The areas occupied by their respective signals were analyzed using the Image J Area measurement tool. Pericyte coverage was quantified as a percentage (%) of CD13-positive pericyte surface area covering lectin-positive capillary

surface area per field (420 × 420 μm). In each animal 5 randomly selected fields from the cortex were analyzed in 6 non-adjacent sections (~100 μm apart).

Smooth-muscle thickness analysis—SM-α staining was performed in PFA fixed tissue sections as described above and signals from axial diving arterioles were subjected to threshold processing. The thickness of the smooth muscle layer was determined by subtracting the diameter of the lumen from the diameter of the lumen and SM-α signal combined. This was done in 4 different angles for each vessel and the average of the 4 was used as the thickness for a given vessel.

Microvascular length measurements—In a few experiments the length of lectin-positive capillary profiles was determined as we have previously reported[9]. Tissue sections were prepared and blocked as described above followed by incubation with *Lycopersicon esculentum* lectin (DL-1174, Dy Light 488, Vector Laboratories). The capillary profile length (vessels < 6 μm in diameter) was measured using the Image J "Neuro J" plug-in length analysis tool from 5 randomly selected fields in the hind limb S1 cortical area (420 × 420 μm) per section from 6 non-adjacent (~100 μm apart) sections per animal, as we described[9]. The length was expressed in mm of lectin-positive vascular profiles per mm^3 of brain tissue.

NeuN-Positive Neuronal Nuclei Counting—NeuN-positive neurons were quantified by using the Image J Cell Counter analysis tool. In each animal 6 randomly selected fields from the cortex were analyzed in 5 nonadjacent sections (~100 μm apart), as we reported[9,54]

SMI-312-Positive Neuritic Density—SMI-312 signals were subjected to threshold processing using Image J. The areas occupied by the signal were then analyzed by a blinded investigator using the Image J Area measurement tool. Total SMI-312-positive area was expressed as a percentage of total brain area in each field. In each animal 6 randomly selected fields from the cortex were analyzed in 5 nonadjacent sections (~100 μm apart), as we reported[9,54].

Aquaporin-4-Positive Astrocyte End-Foot Coverage—Aquaporin-4 and lectin signals from microvessels < 6 μm in diameter were separately subjected to threshold processing. The areas occupied by their respective signals were analyzed using the Image J Area measurement tool. Total aquaporin-4-positive area was expressed as a percentage of total lectin-positive area in each field. In each animal 6 randomly selected fields from the cortex were analyzed in 5 nonadjacent sections (~100 μm apart), as we reported[9].

GFAP-Positive Astrocyte Counting—GFAP-positive astrocytes were quantified by using the Image J Cell Counter analysis tool. In each animal 6 randomly selected fields (420 × 420 μm) from the cortex were analyzed in 5 nonadjacent sections (~100 μm apart), as we reported[9].

Microglia Quantification—The number of Iba1-positive microglia were counted using the Image J Cell Counter analysis tool. In each animal 6 randomly selected fields (420 × 420

μm) from the cortex were analyzed in 5 nonadjacent sections (~100 μm apart), as we reported[9].

Ex Vivo Brain Slice Imaging

Brain slice preparation—Mice were intraorbitally injected with 50 μg Alexa 633 hydrazide (Life Technologies) to identify arterioles[58] and 50 μL *Lycopersicon esculentum* lectin (Vector Laboratories)[9] to identify blood vessels at least 90 min and 30 min, respectively, prior to anesthesia (4% Isofluorane), rapid decapitation and slice preparation on a Leica VT1000S vibratome. Coronal cortical slices (350 μm) containing the hind limb area of the primary somatosensory cortex were cut in ice-cold high-sucrose, low-NaCl aCSF (85mM NaCl, 2.5 mM KCl, 4 mM $MgSO_4$, 0.5 mM $CaCl_2$, 1.25 mM NaH_2PO_4, 25 mM $NaHCO_3$, 25 mM glucose, 74 mM sucrose, 0.5 mM ascorbate and 2 mM kynurenic acid) and stored in a submersion chamber containing normal aCSF (119 mM NaCl, 2.5 mM KCl, 1.3 mM $MgSO_4$, 2.5 mM $CaCl_2$, 1 mM NaH_2PO_4, 26 mM $NaHCO_3$, 11 mM glucose) with 2 mM kynurenic acid, saturated with 95% O_2:5% CO_2, at room temperature. Experiments were performed in a submersion chamber perfused with aCSF and saturated with 95% O_2:5% CO_2.

Imaging of arterioles in live brain slices—Acute brain slices were transferred to a Zeiss Axio Examiner upright DIC fluorescence microscope equipped with a Hamamatsu Orca-Flash 4.0 camera, and images acquired using Zen Pro 2012 software (Carl Zeiss Microimaging). Slices were continually perfused with 95% O_2:5% CO_2 saturated aCSF heated to 37°C. After at least 10 min of acclamation in the recording chamber in aCSF, time lapse images of arterioles were acquired every 5 sec for 22 min (2 min of aCSF, 10 min of 100 μM phenylephrine, 10 min of 400 μM adenosine). Vessel internal diameters were measured at several locations along the vessel using the line capillary tool and peak-to-peak measurement calculation function in ImagePro Premiere software (Media Cybernetics). Experiments and images where focal changes occurred were excluded from analysis. Constriction by phenylephrine values were calculated by comparing the vessel diameter of the last 3 min of phenylephrine application to aCSF baseline measurements. Relaxation by adenosine measurements were calculated by comparing the diameter of the last 3 min of adenosine to the last 3 min of phenylephrine application.

In vivo Microdialysis

In vivo microdialysis was performed to measure lactate and glucose levels in the ISF of isoflurane (~1%) anesthetized mice. An intracerebral guide cannula (Bioanalytical Systems, MBR-5) was stereotaxically implanted over the somatosensory cortex (coordinates: AP −0.5 mm, L −1.5 mm, DV 0 mm) of the mouse. A 1 mm long microdialysis probe (Bioanalytical Systems, MBR 1–5), with 38 KDa molecular weight cutoff, extended from the tip of the cannula into the somatosensory cortex. Artificial cerebrospinal fluid (aCSF; Harvard Apparatus) was continuously perfused through the probe at a flow rate of 0.5 μL/min. After obtaining baseline values for three hours, high-[K^+] (100 mM) aCSF was perfused into the cortex for 60 minutes via retrodialysis to induce local neuronal stimulation. The microdialysates, collected every 30 minutes, were then analyzed for lactate levels (Sigma).

Behavior testing

Novel object recognition (NOR), nesting, and burrowing tests were performed as previously described[59].

Blood pressure measurements

Blood pressure (BP) measurements were performed using a non-invasive tail cuff method (CODA Monitor, Kent Scientific) on isofluorane anesthetized mice under the same conditions and stimulus used for the two-photon diameter and velocity measurements (see above) to confirm BP does not change under those experimental conditions. BP measurements were taken before, at the immediate conclusion of the stimulus, and for several subsequent post-stimulus time points. Mean BP was calculated using the formula: (2/3)Diastolic + (1/3)Systolic pressures. Mean blood pressure (MAP) was 83 ± 7 (mean ± s.e.m.) before stimulus for both 1–2 month old *Pdgfrβ*^{+/−} and littermate control mice, and 83 ± 6 and 84 ± 7 for 1–2 month old *Pdgfrβ*^{+/−} and littermate control mice, respectively, at the conclusion of stimulus.

Statistical analysis

All animals were randomized for their genotype information. Immunostaining experiments were blinded; the operators responsible for the experimental procedures and data analysis were blinded and unaware of group allocation throughout the experiments. Other experiments were analyzed, but not performed, in a blinded fashion. Sample sizes were calculated using nQUERY assuming a two-sided alpha-level of 0.05, 80% power, and homogenous variances for the two samples to be compared, with the means and common standard deviation for different parameters predicted from published data and our previous studies.

All data are expressed as mean ± 95% confidence interval, unless otherwise noted. Grubb's outlier test was used to determine significant outliers, which were excluded from further data analysis (GraphPad). Lilliefors test was used to test normality of the data (XLSTAT). For parametric analysis, the F test was used to determine the equality of variances between the groups compared; statistical significance across two groups was tested by Student's *t*-test (Microsoft Excel 2010). Mann–Whitney U test was used for non-parametric analysis (Prism, GraphPad). Bootstrapping (1,000 sampling size) was performed on data that could not be statistically distinguished from a non-normal distribution to calculate 95% confidence intervals (XLSTAT)[60,61]. Effect size (e.g. Cohen's d) was calculated for all comparisons made (http://www.socscistatistics.com/effectsize/). The accepted level of statistical significance was $p \leq 0.05$.

Supplementary Material

Refer to Web version on PubMed Central for supplementary material.

Acknowledgments

References

1. Attwell D, et al. Glial and neuronal control of brain blood flow. Nature. 2010; 468:232–243. [PubMed: 21068832]

2. Zlokovic BV. Neurovascular pathways to neurodegeneration in Alzheimer's disease and other disorders. Nat. Rev. Neurosci. 2011; 12:723–738. [PubMed: 22048062]

3. Iadecola C. The pathobiology of vascular dementia. Neuron. 2013; 80:844–866. [PubMed: 24267647]

4. Iadecola C, Nedergaard M. Glial regulation of the cerebral microvasculature. Nat. Neurosci. 2007; 10:1369–1376. [PubMed: 17965657]

5. MacVicar BA, Newman EA. Astrocyte regulation of blood flow in the brain. Cold Spring Harb. Perspect. Biol. 2015:7.

6. Rouget C. Memoire sur le developpement, la structures et les proprietes des capillaries sanguins et lymphatiques. Arch Physiol Norm Pathol. 1873; 5:603–633.

7. Armulik A, Genové G, Betsholtz C. Pericytes: developmental, physiological, and pathological perspectives, problems, and promises. Dev. Cell. 2011; 21:193–215. [PubMed: 21839917]

8. Winkler EA, Bell RD, Zlokovic BV. Central nervous system pericytes in health and disease. Nat. Neurosci. 2011; 14:1398–1405. [PubMed: 22030551]

9. Sweeney MD, Ayyadurai S, Zlokovic BV. Pericytes of the neurovascular unit: key functions and signaling pathways. Nat. Neurosci. 2016; 19:771–783. [PubMed: 27227366]

10. Armulik A, et al. Pericytes regulate the blood-brain barrier. Nature. 2010; 468:557–561. [PubMed: 20944627]

11. Daneman R, Zhou L, Kebede AA, Barres BA. Pericytes are required for blood-brain barrier integrity during embryogenesis. Nature. 2010; 468:562–566. [PubMed: 20944625]

12. Bell RD, et al. Pericytes control key neurovascular functions and neuronal phenotype in the adult brain and during brain aging. Neuron. 2010; 68:409–427. [PubMed: 21040844]

13. Peppiatt CM, Howarth C, Mobbs P, Attwell D. Bidirectional control of CNS capillary diameter by pericytes. Nature. 2006; 443:700–704. [PubMed: 17036005]

14. Hall CN, et al. Capillary pericytes regulate cerebral blood flow in health and disease. Nature. 2014; 508:55–60. [PubMed: 24670647]

15. Mishra A, et al. Astrocytes mediate neurovascular signaling to capillary pericytes but not to arterioles. Nat. Neurosci. 2016; 19:1619–1627. [PubMed: 27775719]

16. Fernández-Klett F, Offenhauser N, Dirnagl U, Priller J, Lindauer U. Pericytes in capillaries are contractile in vivo, but arterioles mediate functional hyperemia in the mouse brain. Proc. Natl. Acad. Sci. U. S. A. 2010; 107:22290–22295. [PubMed: 21135230]

17. Hill RA, et al. Regional blood flow in the normal and ischemic brain is controlled by arteriolar smooth muscle cell contractility and not by capillary pericytes. Neuron. 2015; 87:1–16. [PubMed: 26139363]

18. Iadecola C. Neurovascular regulation in the normal brain and in Alzheimer's disease. Nat. Rev. Neurosci. 2004; 5:347–360. [PubMed: 15100718]

19. Montagne A, et al. Blood-brain barrier breakdown in the aging human hippocampus. Neuron. 2015; 85:296–302. [PubMed: 25611508]

20. Farkas E, Luiten PG. Cerebral microvascular pathology in aging and Alzheimer's disease. Prog. Neurobiol. 2001; 64:575–611. [PubMed: 11311463]

21. Baloyannis SJ, Baloyannis IS. The vascular factor in Alzheimer's disease: a study in Golgi technique and electron microscopy. J. Neurol. Sci. 2012; 322:117–121. [PubMed: 22857991]

22. Sengillo JD, et al. Deficiency in mural vascular cells coincides with blood-brain barrier disruption in Alzheimer's disease. Brain Pathol. Zurich Switz. 2013; 23:303–310.

23. Halliday MR, et al. Accelerated pericyte degeneration and blood-brain barrier breakdown in apolipoprotein E4 carriers with Alzheimer's disease. J. Cereb. Blood Flow Metab. Off. J. Int. Soc. Cereb. Blood Flow Metab. 2015

24. Winkler EA, et al. Blood-spinal cord barrier breakdown and pericyte reductions in amyotrophic lateral sclerosis. Acta Neuropathol. (Berl.). 2013; 125:111–120. [PubMed: 22941226]

25. Yemisci M, et al. Pericyte contraction induced by oxidative-nitrative stress impairs capillary reflow despite successful opening of an occluded cerebral artery. Nat. Med. 2009; 15:1031–1037. [PubMed: 19718040]

26. Montagne A, et al. Brain imaging of neurovascular dysfunction in Alzheimer's disease. Acta Neuropathol. (Berl.). 2016; 131:687–707. [PubMed: 27038189]

27. Blinder P, et al. The cortical angiome: an interconnected vascular network with noncolumnar patterns of blood flow. Nat. Neurosci. 2013; 16:889–897. [PubMed: 23749145]

28. Chow N, et al. Serum response factor and myocardin mediate arterial hypercontractility and cerebral blood flow dysregulation in Alzheimer's phenotype. Proc. Natl. Acad. Sci. U. S. A. 2007; 104:823–828. [PubMed: 17215356]

29. Kim TN, et al. Line-scanning particle image velocimetry: an optical approach for quantifying a wide range of blood flow speeds in live animals. PloS One. 2012; 7:e38590. [PubMed: 22761686]

30. Hillman EMC. Optical brain imaging in vivo: techniques and applications from animal to man. J. Biomed. Opt. 2007; 12:051402. [PubMed: 17994863]

31. Sirotin YB, Hillman EMC, Bordier C, Das A. Spatiotemporal precision and hemodynamic mechanism of optical point spreads in alert primates. Proc. Natl. Acad. Sci. U. S. A. 2009; 106:18390–18395. [PubMed: 19828443]

32. Iadecola C, et al. SOD1 rescues cerebral endothelial dysfunction in mice overexpressing amyloid precursor protein. Nat. Neurosci. 1999; 2:157–161. [PubMed: 10195200]

33. Wu Z, et al. Role of the MEOX2 homeobox gene in neurovascular dysfunction in Alzheimer disease. Nat. Med. 2005; 11:959–965. [PubMed: 16116430]

34. Sakadžić S, et al. Two-photon high-resolution measurement of partial pressure of oxygen in cerebral vasculature and tissue. Nat. Methods. 2010; 7:755–759. [PubMed: 20693997]

35. Kasischke KA, et al. Two-photon NADH imaging exposes boundaries of oxygen diffusion in cortical vascular supply regions. J. Cereb. Blood Flow Metab. Off. J. Int. Soc. Cereb. Blood Flow Metab. 2011; 31:68–81.

36. Baraghis E, et al. Two-photon microscopy of cortical NADH fluorescence intensity changes: correcting contamination from the hemodynamic response. J. Biomed. Opt. 2011; 16:106003. [PubMed: 22029350]

37. Dromparis P, Michelakis ED. Mitochondria in vascular health and disease. Annu. Rev. Physiol. 2013; 75:95–126. [PubMed: 23157555]

38. Barros LF. Metabolic signaling by lactate in the brain. Trends Neurosci. 2013; 36:396–404. [PubMed: 23639382]

39. Ishii Y, et al. Characterization of neuroprogenitor cells expressing the PDGF beta-receptor within the subventricular zone of postnatal mice. Mol. Cell. Neurosci. 2008; 37:507–518. [PubMed: 18243733]

40. Lindahl P, Johansson BR, Levéen P, Betsholtz C. Pericyte loss and microaneurysm formation in PDGF-B-deficient mice. Science. 1997; 277:242–245. [PubMed: 9211853]

41. Winkler EA, Bell RD, Zlokovic BV. Pericyte-specific expression of PDGF beta receptor in mouse models with normal and deficient PDGF beta receptor signaling. Mol. Neurodegener. 2010; 5:32. [PubMed: 20738866]

42. Hartmann DA, et al. Pericyte structure and distribution in the cerebral cortex revealed by high-resolution imaging of transgenic mice. Neurophotonics. 2015; 2:041402. [PubMed: 26158016]

43. Attwell D, Mishra A, Hall CN, O'Farrell FM, Dalkara T. What is a pericyte? J. Cereb. Blood Flow Metab. Off. J. Int. Soc. Cereb. Blood Flow Metab. 2016; 36:451–455.

44. Winkler EA, Sagare AP, Zlokovic BV. The pericyte: a forgotten cell type with important implications for Alzheimer's disease? Brain Pathol. Zurich Switz. 2014; 24:371–386.

45. Kawamura H, et al. Effects of angiotensin II on the pericyte-containing microvasculature of the rat retina. J. Physiol. 2004; 561:671–683. [PubMed: 15486015]

46. Yamanishi S, Katsumura K, Kobayashi T, Puro DG. Extracellular lactate as a dynamic vasoactive signal in the rat retinal microvasculature. Am. J. Physiol. Heart Circ. Physiol. 2006; 290:H925–H934. [PubMed: 16299264]

47. Oishi K, Kamiyashiki T, Ito Y. Isometric contraction of microvascular pericytes from mouse brain parenchyma. Microvasc. Res. 2007; 73:20–28. [PubMed: 17030042]

48. Dai M, Nuttall A, Yang Y, Shi X. Visualization and contractile activity of cochlear pericytes in the capillaries of the spiral ligament. Hear. Res. 2009; 254:100–107. [PubMed: 19422897]

49. Park L, et al. Age-dependent neurovascular dysfunction and damage in a mouse model of cerebral amyloid angiopathy. Stroke J. Cereb. Circ. 2014; 45:1815–1821.

50. Takano T, et al. Astrocyte-mediated control of cerebral blood flow. Nat. Neurosci. 2006; 9:260–267. [PubMed: 16388306]

51. Ragan T, et al. Serial two-photon tomography for automated ex vivo mouse brain imaging. Nat. Methods. 2012; 9:255–258. [PubMed: 22245809]

52. Tsai PS, et al. Correlations of neuronal and microvascular densities in murine cortex revealed by direct counting and colocalization of nuclei and vessels. J. Neurosci. Off. J. Soc. Neurosci. 2009; 29:14553–14570.

53. Brown CE, Aminoltejari K, Erb H, Winship IR, Murphy TH. In vivo voltage-sensitive dye imaging in adult mice reveals that somatosensory maps lost to stroke are replaced over weeks by new structural and functional circuits with prolonged modes of activation within both the peri-infarct zone and distant sites. J. Neurosci. Off. J. Soc. Neurosci. 2009; 29:1719–1734.

54. Bell RD, et al. Apolipoprotein E controls cerebrovascular integrity via cyclophilin A. Nature. 2012; 485:512–516. [PubMed: 22622580]

55. Harrison TC, Sigler A, Murphy TH. Simple and cost-effective hardware and software for functional brain mapping using intrinsic optical signal imaging. J. Neurosci. Methods. 2009; 182:211–218. [PubMed: 19559049]

56. Frostig RD, Lieke EE, Ts'o DY, Grinvald A. Cortical functional architecture and local coupling between neuronal activity and the microcirculation revealed by in vivo high-resolution optical imaging of intrinsic signals. Proc. Natl. Acad. Sci. 1990; 87:6082–6086. [PubMed: 2117272]

57. Winkler EA, Bell RD, Zlokovic BV. Pericyte-specific expression of PDGF beta receptor in mouse models with normal and deficient PDGF beta receptor signaling. Mol. Neurodegener. 2010; 5:32. [PubMed: 20738866]

58. Shen Z, Lu Z, Chhatbar PY, O'Herron P, Kara P. An artery-specific fluorescent dye for studying neurovascular coupling. Nat. Methods. 2012; 9:273–276. [PubMed: 22266543]

59. Sagare AP, et al. Pericyte loss influences Alzheimer-like neurodegeneration in mice. Nat. Commun. 2013; 4:2932. [PubMed: 24336108]

60. Hesterberg T. Bootstrap. Wiley Interdiscip. Rev. Comput. Stat. 2011; 3:497–526.

61. Efron, B., Tibshirani, R. An introduction to the bootstrap. Chapman & Hall: 1993.

62. Winkler EA, Sengillo JD, Bell RD, Wang J, Zlokovic BV. Blood-spinal cord barrier pericyte reductions contribute to increased capillary permeability. J. Cereb. Blood Flow Metab. Off. J. Int. Soc. Cereb. Blood Flow Metab. 2012; 32:1841–1852.

63. Winkler EA, et al. GLUT1 reductions exacerbate Alzheimer's disease vasculo-neuronal dysfunction and degeneration. Nat. Neurosci. 2015; 18:521–530. [PubMed: 25730668]

64. Li T, et al. The neuritic plaque facilitates pathological conversion of tau in an Alzheimer's disease mouse model. Nat. Commun. 2016; 7:12082. [PubMed: 27373369]

65. Wang Y, et al. 3K3A–activated protein C stimulates postischemic neuronal repair by human neural stem cells in mice. Nat. Med. 2016; 22:1050–1055. [PubMed: 27548576]

66. Goodpaster T, Randolph-Habecker J. A flexible mouse-on-mouse immunohistochemical staining technique adaptable to biotin-free reagents, immunofluorescence, and multiple antibody staining. J. Histochem. Cytochem. Off. J. Histochem. Soc. 2014; 62:197–204.
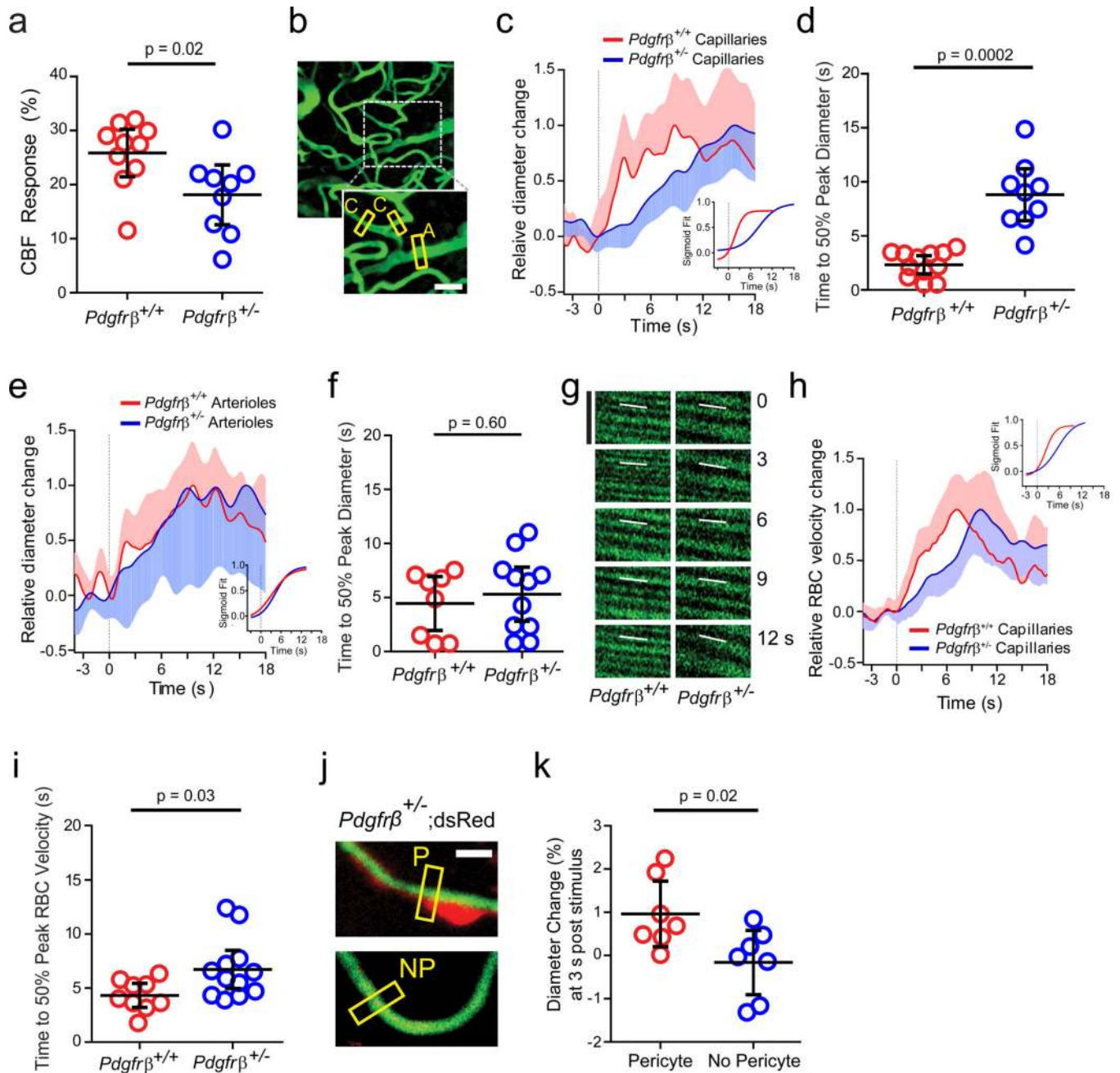
Figure 1. Delayed capillary dilation and reduced capillary red blood cell flow in response to a hind limb stimulus in 1–2 month old pericyte-deficient *Pdgfrβ*^{+/−} mice

(**a**) Cerebral blood flow (CBF) response to an electrical hind limb stimulus (60 s, 7 Hz, 2 ms pulse duration) determined by laser doppler flowmetry (LDF) as a percentage of baseline change in *Pdgfrβ*^{+/−} mice (n=9) and age-matched *Pdgfrβ*^{+/+} (n=10) littermate controls. Circles denote individual values derived from 3 independent LDF measurements per mouse; mean ± 95% confidence interval (CI); t-test, equal variances: t = 2.52, p = 0.02. (**b**) Representative z-stack projection of capillary (C) and arteriole (A) diameter measurement locations by TPLSM (inset; yellow boxes). Scale bar = 20 μm. (**c**) Time courses of diameter changes (mean ± 95% CI) in capillaries in *Pdgfrβ*^{+/+} (red; n=12 mice; 37 total capillaries)

and *Pdgfrβ*^{+/−} (blue; n=9 mice, 33 total capillaries) mice in the hind limb S1 cortical area after an electrical hind limb stimulus (10 s, 10 Hz, 2 ms pulse duration). Diameter changes are expressed relative to the respective basal capillary diameter prior to stimulation (value set as 0) and maximal diameter after stimulation (value set as 1). Vertical line denotes initiation of stimulus. Inset: sigmoid curve fits to the *Pdgfrβ*^{+/+} (red) and *Pdgfrβ*^{+/−} (blue) time courses show average capillary diameter increase during the overall time course of dilation. (**d**) Average time (mean ± 95% CI) to 50% peak capillary diameter dilation increase in *Pdgfrβ*^{+/+} (red; n=12 mice; 37 total capillaries) and *Pdgfrβ*^{+/−} (blue; n=9 mice; 33 total capillaries) mice from **c** (t-test, unequal variance: t = 6.48, p = 0.0002). Circles represent values per mouse derived from averaging individual capillary responses from sigmoid parametric fits to each capillary time course of dilation increase. (**e**) Time courses of diameter changes in arterioles in *Pdgfrβ*^{+/+} (red; n=8 mice; 18 total arterioles) and *Pdgfrβ*^{+/−} (blue; n=11 mice; 20 total arterioles) mice in S1 cortex, in response to an electrical hind limb stimulus (10 s, 10 Hz, 2 ms pulse duration). Arteriolar diameter changes are expressed relative to the respective basal and maximal diameter prior to and after stimulation, respectively, as for capillaries in **c**. Vertical line denotes initiation of stimulus. Inset: sigmoid curve fits to the *Pdgfrβ*^{+/+} (red) and *Pdgfrβ*^{+/−} (blue) average arteriole diameter increase during the overall time course of dilation increase. (**f**) Average time (mean ± 95% CI) to 50% peak arteriole diameter dilation increase in *Pdgfrβ*^{+/−} mice (blue; n=8 mice; 18 total arterioles) and *Pdgfrβ*^{+/+} mice (red; n=11 mice; 20 total arterioles) (t-test, equal variance: t = 0.54, p = 0.60). Circles represent values per mouse derived from averaging the individual arteriolar responses. Time to 50% peak diameter increase was determined from individual sigmoid parametric fits to each arteriole time course of dilation increase. (**g**) Representative red blood cell (RBC) TPLSM capillary linescans from *Pdgfrβ*^{+/−} and *Pdgfrβ*^{+/+} capillaries illustrating RBC velocity changes after an electrical hind limb stimulus (10 s, 10 Hz, 2 ms pulse duration). Dark lines closer to horizontal reflect faster RBCs. White lines: visual reference along RBC trajectories. Scale bar (left) = 0.35 s. (**h**) Time courses of stimulus-driven RBC velocity changes in capillaries (mean ± 95% CI) from *Pdgfrβ*^{+/+} (red; n=12 mice; 38 total capillaries) and *Pdgfrβ*^{+/−} (blue; n=9 mice; 39 total capillaries) mice. RBC velocity changes are expressed relative to the respective basal RBC velocity prior to stimulation (value set as 0) and maximal velocity upon stimulation (value set as 1). Vertical line denotes initiation of stimulus. Inset: sigmoid curve fits to the *Pdgfrβ*^{+/+} (red) and *Pdgfrβ*^{+/−} (blue) average capillary RBC velocity increase during the overall time course of velocity increase. (**i**) Average time (mean ± 95% CI) to 50% peak RBC capillary velocity increase in *Pdgfrβ*^{+/+} (red; n=12 mice; 38 total capillaries) and *Pdgfrβ*^{+/−} (blue; n=9 mice; 39 total capillaries) mice from **h** (t-test, equal variance: t = 2.35, p = 0.030). Circles represent values per mouse derived from averaging the individual RBC capillary velocity increase per mouse. Time to 50% peak RBC velocity increase was determined from sigmoid parametric fits of individual capillary time courses utilizing the overall time course of RBC velocity increase. (**j**) Representative measurement locations on capillaries either covered by a pericyte (P, red, top) or in the absence of a pericyte (NP, bottom) in *Pdgfrβ*^{+/−} mice crossed with NG2-dsRed mice (*Pdgfrβ*^{+/−};dsRed). Scale bar = 10 μm. (**k**) Relative dilation of pericyte-present and pericyte-absent capillary segments after an electrical hind limb stimulus (10 s, 10 Hz, 2 ms pulse duration) in *Pdgfrβ*^{+/−};dsRed mice determined at 3 s after stimulus initiation. Responses (mean ± 95% CI) from 7 mice at 33 total pericyte-present (red) and 34

total pericyte-absent (blue) capillaries. Circles denote individual values per mouse derived from averaging all individual capillary dilation values per mouse per condition (t test, equal variance: t = 2.59, p = 0.02). P values by two-tail t-tests used as indicated for each dataset in the legend for panels a, d, f, i, and k.
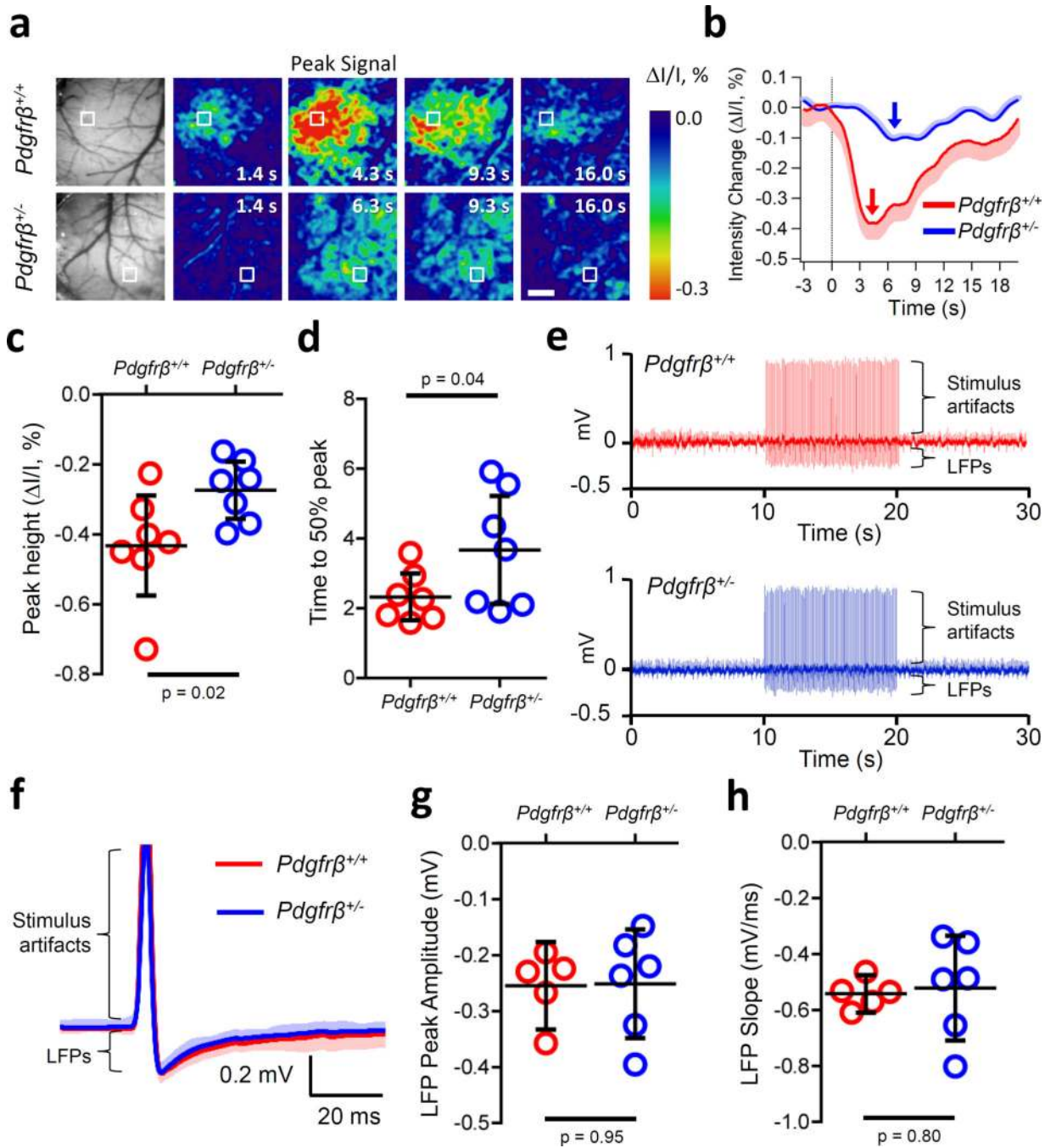
Figure 2. Impaired hemodynamic response in 1–2 month old pericyte-deficient *Pdgfrβ*^{+/−} mice determined by intrinsic optical signal (IOS) imaging (530 nm) at a time-point when neuronal activity is unaffected as determined by local field potential (LFP) recordings

(**a**) Example grayscale images of the visualized somatosensory cortex showing vasculature (far left) and IOS signals under 530 nm illumination (pseudocolored) in response to an electrical hind limb stimulus (10 s, 10 Hz, 2 ms pulse duration) beginning at 0 s in *Pdgfrβ*^{+/−} mice and *Pdgfrβ*^{+/+} littermate controls. Peak signals and peak signal times are indicated. Scale bar = 0.5 mm. Boxes indicate regions of interests (ROIs) at least 30 μm away from large surface blood vessels for data shown in panel **b**. (**b**) IOS signal time courses in

parenchymal regions for the examples shown in boxed ROIs in **a**. Arrows denote peak IOS signal times for $Pdgfr\beta^{+/-}$ (red) and littermate control $Pdgfr\beta^{+/+}$ (blue) mice. Curves are averages of 10 trials for a representative individual mouse (mean ± 95% CI) per group. (**c,d**) Average (mean ± 95% CI) change in IOS peak height (t-test, equal variance, single tail: t = 2.35, p = 0.02) (**c**), and time to 50% peak response signal (t-test, equal variance, single tail: t = 1.95, p = 0.04) (**d**) in 7 $Pdgfr\beta^{+/+}$ and 7 $Pdgfr\beta^{+/-}$ mice in ROIs away from large surface vessels. Each circle represents the value per mouse averaged from 10 trials as shown in **b**. (**e**) Representative traces from single trials illustrating a train of evoked LFPs. After a 10 s baseline, hindlimb stimulus was applied (10 s, 10 Hz, 0.1 ms pulse duration) followed by a 10 s run out in $Pdgfr\beta^{+/+}$ (top, red) and $Pdgfr\beta^{+/-}$ (bottom, blue) mice. (**f**) 100 averaged LFP traces from a single trial (mean ± 95% CI) for $Pdgfr\beta^{+/+}$ (red) and $Pdgfr\beta^{+/-}$ (blue) mice shown in **e**. Stimulus artifacts and LFPs are indicated in **e** and **f**. (**g**) Average (mean ± 95% CI) peak amplitude (t-test, equal variance: t = 0.07, p = 0.95) and (**h**) slope (t-test, unequal variance: t = 0.12, p = 0.80) from $Pdgfr\beta^{+/+}$ (n=5 mice; 2,500 total LFPs) and $Pdgfr\beta^{+/-}$ (n=6 mice; 3,600 total LFPs) mice. Two-tail t-tests used unless otherwise indicated.
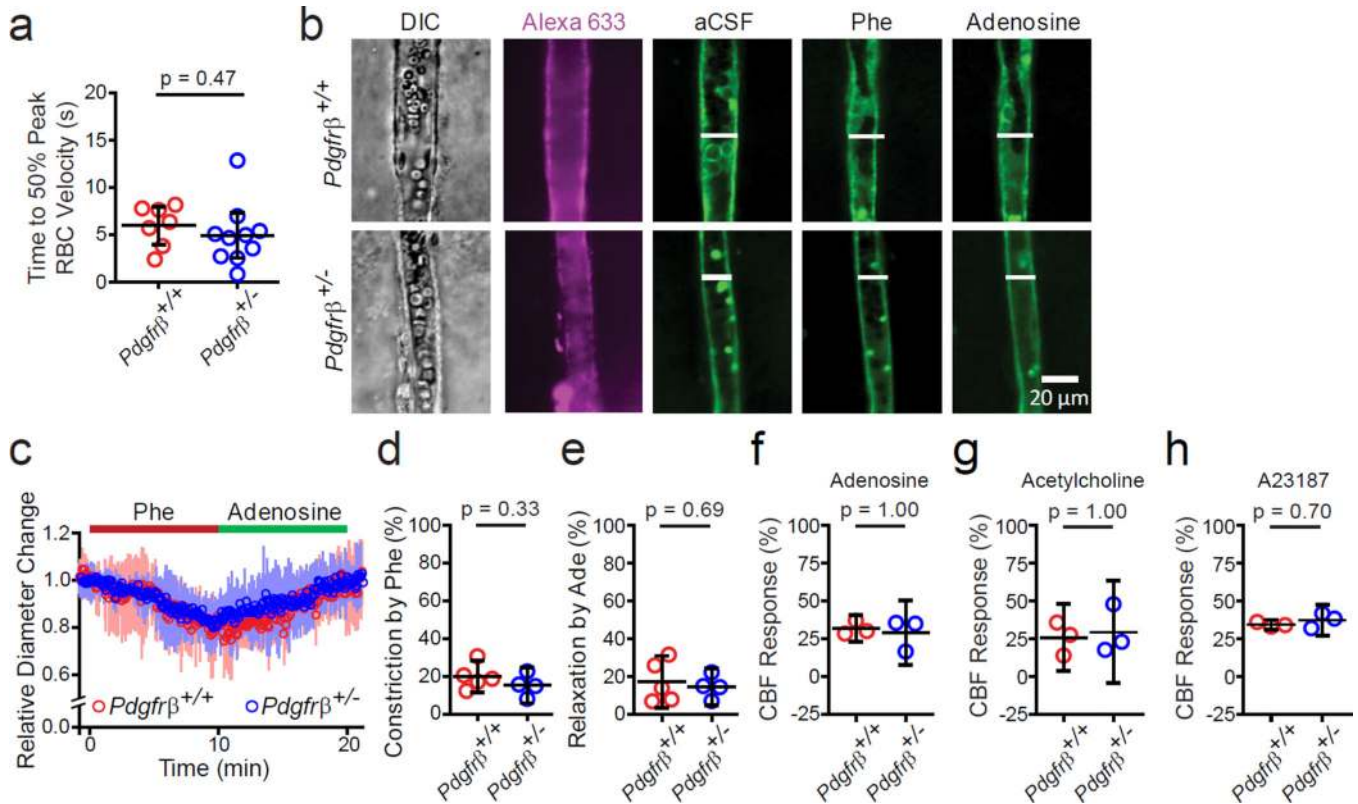
Figure 3. Arteriolar vasoactivity and endothelial-dependent vasodilation in 1–2 month old pericyte-deficient *Pdgfrβ*$^{+/-}$ mice and age-matched littermate controls

(**a**) Average time (mean ± 95% CI) to 50% peak arteriole RBC velocity increase *in vivo* from 10 *Pdgfrβ*$^{+/-}$ mice (24 total arterioles) and 7 *Pdgfrβ*$^{+/+}$ mice (14 total arterioles) (t-test, equal variance: t = 0.74, p = 0.47) after an electrical hind limb stimulus (10 s, 10 Hz, 2 ms pulse duration) as in Fig. 1g–i. Circles denote individual values per mouse derived from averaging all times to 50% peak arteriolar RBC velocity increase per mouse. (**b**) Representative measurement of arteriole smooth muscle cell function in brain slices in the cortical S1 region in *Pdgfrβ*$^{+/+}$ and *Pdgfrβ*$^{+/-}$ mice in resting conditions (aCSF, artificial cerebrospinal fluid), and after 100 μM phenylephrine (Phe; constriction) and 400 μM adenosine (relaxation). DIC: differential interference contrast bright field image. Alexa633: Arteriole-specific vessel marker confirming vessel type. (**c**) Average (mean ± 95% CI) arteriole diameter change relative to basal value in brain slices from 5 *Pdgfrβ*$^{+/+}$ mice and 4 *Pdgfrβ*$^{+/-}$ mice. (**d-e**) Quantification (mean ± 95% CI) of arteriole constriction by phenylephrine (t-test, equal variance: t = 1.05, p = 0.33) (**d**) and relaxation by adenosine (t-test, equal variance: t = 0.41, p = 0.69) (**e**) in brain slices from 5 *Pdgfrβ*$^{+/+}$ and 4 *Pdgfrβ*$^{+/-}$ mice: data from 2–3 slices were averaged per mouse. (**f-h**) *In vivo* cerebral blood flow (CBF) response to adenosine (400 μM; Mann-Whitney U test,, p=1.00) (**f**), acetylcholine (10 μM; Mann-Whitney U test, p=1.00) (**g**) and A23187 (3 μM; Mann-Whitney U test, p=0.70) (**h**) determined by laser Doppler flowmetry in 3 *Pdgfrβ*$^{+/+}$ and 3 *Pdgfrβ*$^{+/-}$ mice. Vasoactive agents were superfused over the exposed cortical surface. LDF measurements were performed in triplicate and an average individual value per animal was used for statistical analysis. Two-tail t-tests used unless otherwise indicated. Bootstrapped in panels **f–h**.
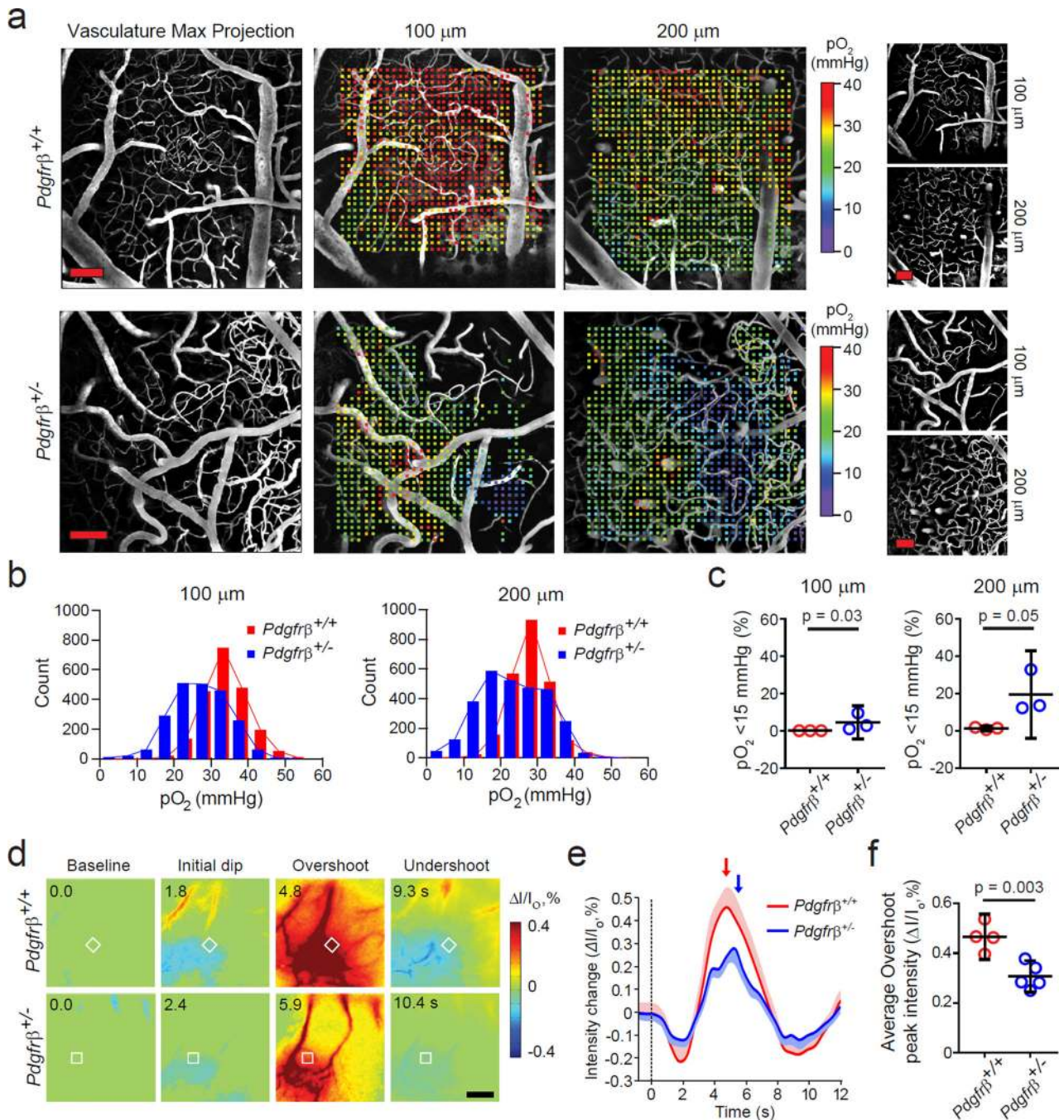
Figure 4. Diminished brain tissue oxygen levels and oxygen delivery in young pericyte-deficient *Pdgfrβ+/−* mice

(**a**) Representative maximal intensity plots of rhodamine-labeld vasculature (left) and oxygen partial pressure (pO$_2$) measurements for the same cortical regions at two different depths in 5–6 month old *Pdgfrβ+/+* and *Pdgfrβ+/−* mice. Far right: Maximal intensity projection examples of the vasculature within the first 100 μm depth, and between 100–200 μm depth. Scale bars = 100 μm. (**b**) Histograms of distribution of pO$_2$ measurements at 100 μm (left) and 200 μm (right) depth between 0 and 60 mm Hg. A total of 2076 measurements

at 100 μm and 2344 measurements at 200 μm for *Pdgfrβ*^{+/+} mice and a total of 2173 measurements at 100 μm and 2867 measurements at 200 μm for *Pdgfrβ*^{+/−} mice were pooled from 3 mice in each group. (**c**) Percent of image fields with pO_2 values < 15 mmHg at 100 μm (left) and 200 μm (right) depth (mean ± 95% CI) from 3 mice per group. Individual values were obtained from 381–1016 measurements per mouse per depth (Mann-Whitney U-test, single tail: p = 0.03 at 100 μm and p = 0.05 at 200 μm; bootstrapped at both depths). (**d**) Pseudocolored IOS image sequence illustrating the activity map in the S1 region in response to hind limb stimulation (300 ms mechanical vibration stimulus), showing baseline and peak responses of different phases including the initial dip (negative), followed by overshoot (positive peak), and undershoot (second negative deflection). Data were obtained using 627 nm illumination in 1–2 month old *Pdgfrβ*^{+/+} and *Pdgfrβ*^{+/−} mice. Blues are negative signals and reds are positive signals. Scale bar = 0.5 mm. (**e**) Example IOS signal traces of intensity change in response to stimulus (at t = 0.0 s) from the ROIs (box locations, at least 30 μm away from large surface blood vessels) of images shown in **d**. Curves are averages of 10 trials for a representative individual mouse (mean ± 95% CI) per group. Arrows indicate the peaks of overshoot. (**f**) Quantification (mean ± 95% CI) of average peak intensity of the overshoot response (arrows in panel **e**) in 4 *Pdgfrβ*^{+/+} and 5 *Pdgfrβ*^{+/−} mice (t-test, two-tail, equal variance: t = 4.39, p = 0.003).
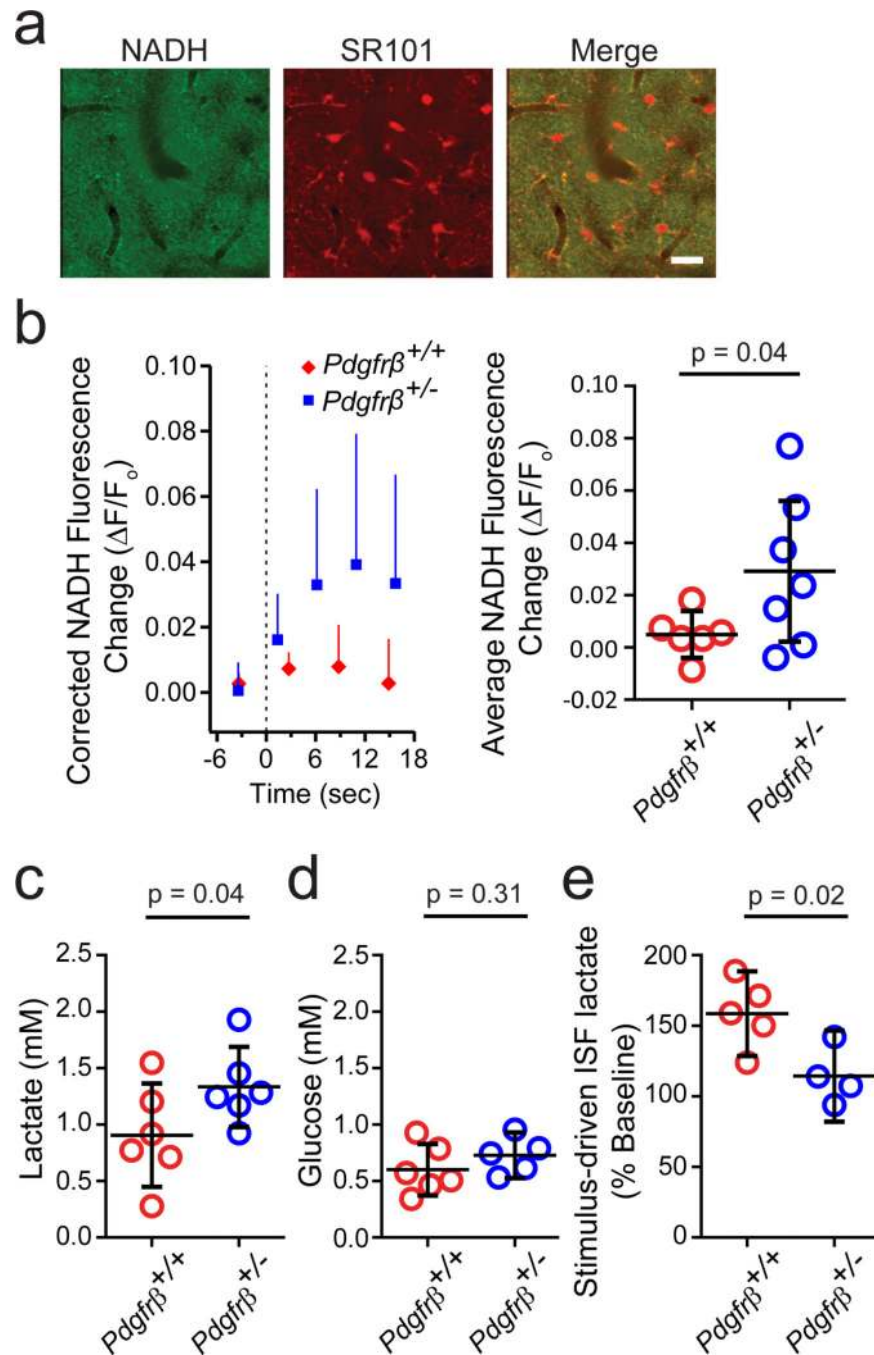
Figure 5. Metabolic changes in 1–2 month old pericyte-deficient $Pdgfr\beta^{+/-}$ mice

(**a**) Representative images of NADH and SR101 measurements. Astrocyte somas appear as bright spots in the SR101 image. Scale bar = 20 μm. (**b**) Stimulus-induced SR101-corrected NADH signals (*left*), and average SR101-corrected NADH signal (*right*; mean ± 95% CI) in 6 $Pdgfr\beta^{+/+}$ and 7 $Pdgfr\beta^{+/-}$ mice (t-test, single tail, unequal variance: t = 1.81, p = 0.04) after an electrical hind limb stimulation (10 s, 10 Hz, 2 ms pulse duration) as in Fig. 1c–e. and Fig. 2a. (**c-e**) Microdialysis measurements (mean ± 95% CI) of cortical resting state interstitial fluid (ISF) lactate concentration in 6 $Pdgfr\beta^{+/+}$ and 5 $Pdgfr\beta^{+/-}$ mice (t-test,

single tail, equal variance: t = 1.90, p = 0.04) (**c**), resting state ISF glucose concentration in 6 *Pdgfrβ*$^{+/+}$ and 5 *Pdgfrβ*$^{+/−}$ mice (t-test, equal variance: t = 1.08, p = 0.31) (**d**), and the percent change in stimulus-driven cortical ISF lactate concentration compared to the baseline levels in 5 *Pdgfrβ*$^{+/+}$ mice and 4 *Pdgfrβ*$^{+/−}$ mice after potassium chloride retrodialysis (t-test, equal variance: t = 2.91, p = 0.02) (**e**). Two-tail t-tests used unless otherwise indicated.
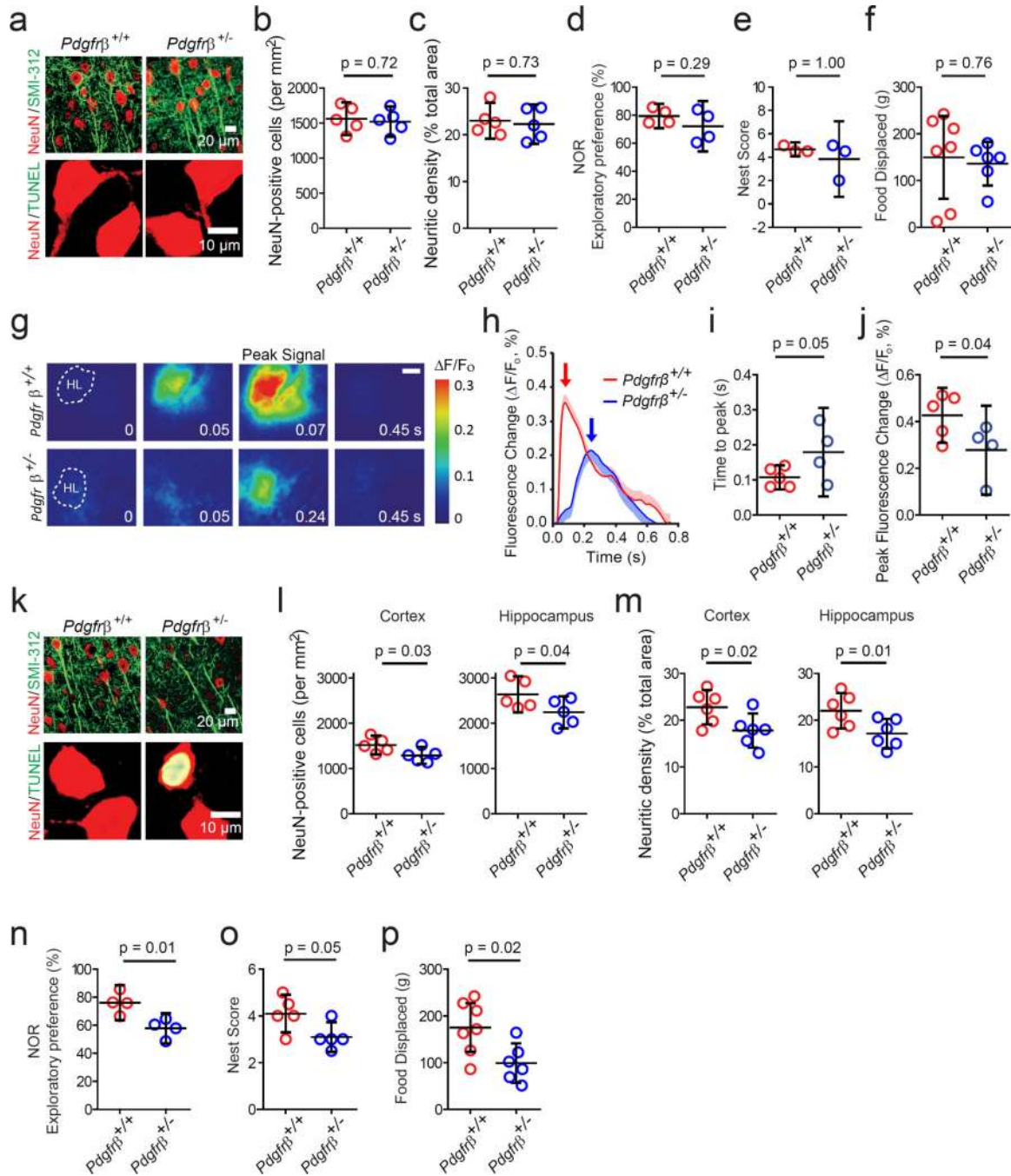
Figure 6. Cortical neuronal activity, neuronal number, neuritic density and behavior in 1–2 and 6–8 month old pericyte-deficient *Pdgfrβ*+/− mice and age-matched littermate controls

(**a**) Double immunostaining for NeuN (neuronal marker) and SMI-312-positive neurofilament (top), and NeuN and TUNEL (bottom) in 1–2 month old *Pdgfrβ*+/+ and *Pdgfrβ*+/− mice. (**b-c**) Quantification (mean ± 95% CI) of NeuN-positive cells (t-test, equal variance: t = 0.37, p = 0.72) (**b**) and SMI-312-positive neuritic density (t-test, equal variance: t = 0.35, p = 0.73) (**c**) in the S1 cortex in 5 *Pdgfrβ*+/+ and 5 *Pdgfrβ*+/− mice at 1–2 months of age. In each animal 6 randomly selected fields from the cortex were analyzed in 5

nonadjacent sections (~100 μm apart) and data were averaged per mouse to obtain individual values (circles) as illustrated. (**d-f**) Novel object recognition (NOR) (**d**, n = 4 mice per group; t-test, equal variance: t = 1.17, p = 0.29), nest construction (**e**, n = 3 mice per group; Mann-Whitney U test, p = 1.00), and burrowing (**f**, food displacement; 7 *Pdgfrβ*$^{+/+}$ and 6 *Pdgfrβ*$^{+/−}$ mice; t-test, equal variance: t = 0.31, p = 0.76) in 1–2 month old mice; all values are mean ± 95% CI. (**g**) Representative pseudo-colored voltage-sensitive dye (VSD) image sequence of cortical neuronal activity in response to a 300 ms hind limb mechanical stimulus in 6–8 mo old *Pdgfrβ*$^{+/+}$ and *Pdgfrβ*$^{+/−}$ mice. Hind limb (HL) region is indicated by dashed line. Scale bar = 0.5 mm. (**h-j**) Representative VSD intensity traces (**h**), time to peak (**i**, t-test, single tail, equal variance: t = 1.91, p = 0.05) and peak fluorescence change (**j**; mean ± CI.; t-test, single tail, equal variance: t = 2.09, p = 0.04) in 5 *Pdgfrβ*$^{+/+}$ and 4 *Pdgfrβ*$^{+/−}$ mice at 6–8 months of age. Arrows in (**h**) indicate peak VSD signal times for 6–8 month old *Pdgfrβ*$^{+/−}$ mice (blue) and *Pdgfrβ*$^{+/+}$ (red) controls. Curves are averages of 10 trials for a representative individual mouse (mean ± 95% CI) per group. VSD data showing no changes in cortical neuronal activity in 1–2 month old *Pdgfrβ*$^{+/−}$ mice are shown in Supplementary Fig. 7. (**k**) Double immunostaining for NeuN (neuronal marker) and SMI-312-positive neurofilament (top), and NeuN and TUNEL (bottom) in S1 cortex in 6–8 month old mice. (**l-m**) Quantification (mean ± 95% CI) of NeuN-positive cells (**l**, cortex: t-test, single tail, equal variance: t = 2.28, p = 0.03; hippocampus: t-test, equal variance: t = 2.05, p = 0.04) in 5 *Pdgfrβ*$^{+/+}$ and 5 *Pdgfrβ*$^{+/−}$ mice, and SMI-312-positive neuritic density (**m**, cortex: t-test, single tail, equal variance: t = 2.48, p = 0.02; hippocampus: t-test, single tail, equal variance: t = 2.56, p = 0.01) in the S1 cortex and CA1 hippocampus in 6 *Pdgfrβ*$^{+/+}$ and 6 *Pdgfrβ*$^{+/−}$ mice at 6–8 months of age. In each animal 6 randomly selected fields from the cortex were analyzed in 5 nonadjacent sections (~100 μm apart) and data were averaged per mouse to obtain individual values (circles) as illustrated. (**n-p**) NOR (**n**, n = 4 mice per group; t-test, equal variance: t = 3.52, p = 0.01), nest construction (**o**, n = 5 mice per group; Mann-Whitney U test, single tail, p = 0.05), and burrowing (**p**, food displacement; 7 *Pdgfrβ*$^{+/+}$ and 6 *Pdgfrβ*$^{+/−}$; t-test, equal variance: t = 2.76, p = 0.02) in 6–8 month old mice. All values are mean ± 95% CI. Two-tail t-tests used unless otherwise indicated. Bootstrapped in panels **e,o**.